広島大学 学位論文

Presence of the Electric Dipole Moment in Quantum Paraelectric SrTiO$_3$ Probed using Resonant X-ray Emission Spectroscopy

共鳴 **X** 線発光分光測定で捉えた
量子常誘電体 **SrTiO$_3$** に誘起される電気双極子モーメント

2016 年

広島大学大学院理学研究科
物理科学専攻

川上 修平

Doctoral Thesis

Presence of the Electric Dipole Moment in Quantum Paraelectric SrTiO$_3$ Probed using Resonant X-ray Emission Spectroscopy

Shuhei Kawakami

Graduate School of Science

Hiroshima University

2016

- **Abstract**

Below a temperature of 40 K, SrTiO$_3$, known as a typical perovskite-structured material, shows quantum paraelectricity with suppression of the ferroelectric state by a quantum fluctuation. In the quantum paraelectric (QPE) phase, the local symmetry around a Ti atom is expected to be reduced by external stimuli such as ultraviolet (UV) light and direct-current (DC) electric field. Although the physical properties of QPE SrTiO$_3$ under external stimuli have been studied by many researchers, the evidence of the electric dipole moment presence in a unit cell remains unclear. In this study, the electric dipole moment resulting from Ti off-center displacement in SrTiO$_3$ and its behavior under UV irradiation and a DC field are revealed using resonant X-ray emission spectroscopy (RXES). The element specificity and orbital selectivity of RXES are useful to probe the electronic structure around a Ti atom, which is expected to change with Ti off-center displacement.

For a SrTiO$_3$ single crystal in the QPE phase, Ti-L and $K\beta$ RXES measurements are performed under UV irradiation and a DC field. The obtained RXES spectra provide the information about crystal-field (dd) and charge-transfer (CT) excitations influenced by p–d hybridization between Ti-$3d$ and O-$2p$ orbitals. As a major result, the RXES measurements show that a Ti atom is displaced from the body-center site of the TiO$_6$ octahedron at low temperature. The electric dipole moment hidden by a quantum fluctuation is directly detected by observing the change of CT excitation. In addition, UV irradiation leads to an increase of Ti off-center displacement, and the UV-induced electric dipole moments evolve into polar regions owing to DC field application. It is clarified that Ti off-center displacement in the QPE phase is developed due to external stimuli and that it is the origin of polar regions. The author confirms that RXES contributes to the investigation of the microscopic nature of dielectric materials.

Contents

1. Introduction

1.1. Physical Properties of SrTiO₃

1.1.1. Characteristics

SrTiO$_3$, known as an ABO_3 perovskite oxide, is a typical band insulator. The crystal structure is cubic with space group $Pm\bar{3}m$ at room temperature, and its lattice constant is 3.905 Å (**Figure 1-1**). The direct and indirect band-gap energies between Ti-$3d$ conduction band and O-$2p$ valence band are 3.4 and 3.2 eV, respectively. This crystal is a useful substrate material because of its high chemical stability.

SrTiO$_3$ has also been studied with regard to various properties such as superconductivity [1] and the giant Seebeck effect. [2] Recently, two-dimensional electron gas (2DEG) with a high mobility has been discovered on the SrTiO$_3$ surface [3, 4] and at the LaAlO$_3$/SrTiO$_3$ heterointerface. [5] At low temperatures, ultraviolet (UV) irradiation with a photon energy greater than the optical band gap of SrTiO$_3$ induces intriguing properties such as visible luminescence and enhancement of the dielectric constant. SrTiO$_3$ is a fluorescent material that emits visible light under UV irradiation. Stoichiometric SrTiO$_3$ emits greenish light at low temperature, whereas lanthanum-doped or oxygen-deficient SrTiO$_3$ emits blue light at room temperature. [6, 7]
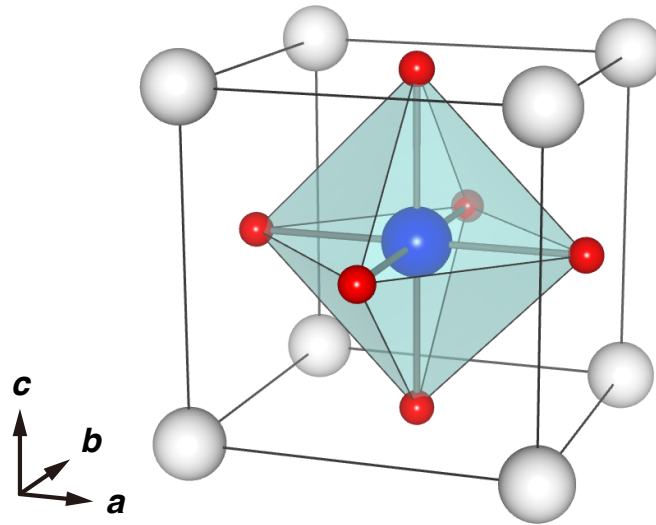
Figure 1-1. Unit cell of $SrTiO_3$ is a perfect cube at room temperature. A Ti atom (blue ball) at the body center is surrounded by six equivalent O atoms (red balls)

• **Splitting of 3*d* Electronic State**

d orbital of a transition metal has normally quintuple degeneracy. In case of $SrTiO_3$, 3*d* orbitals of Ti under O_h symmetry are split into triply-degenerated t_{2g} components and doubly-degenerated e_g components by the coulomb potential of the anion (O^{2-}), i.e., crystal field splitting [**Figure 1-2(a)**]. The energy gap between t_{2g} and e_g states is characterized using crystal field parameter $10Dq$. Each limb of t_{2g} orbitals (*xy*, *yz*, *zx*) is pointing to the according edge of the cubic lattice, away from the oxygen site. In contrast, each limb of e_g orbitals (x^2-y^2, $3z^2-r^2$) extends towards the oxygen site [**Figure 1-2(b)**].

(a)

e_g

$3d$

$10Dq$

t_{2g}

(b)

e_g **orbitals**

$3z^2\text{-}r^2$ z

$x^2\text{-}y^2$ z

t_{2g} **orbitals**

xy z

yz z

zx z
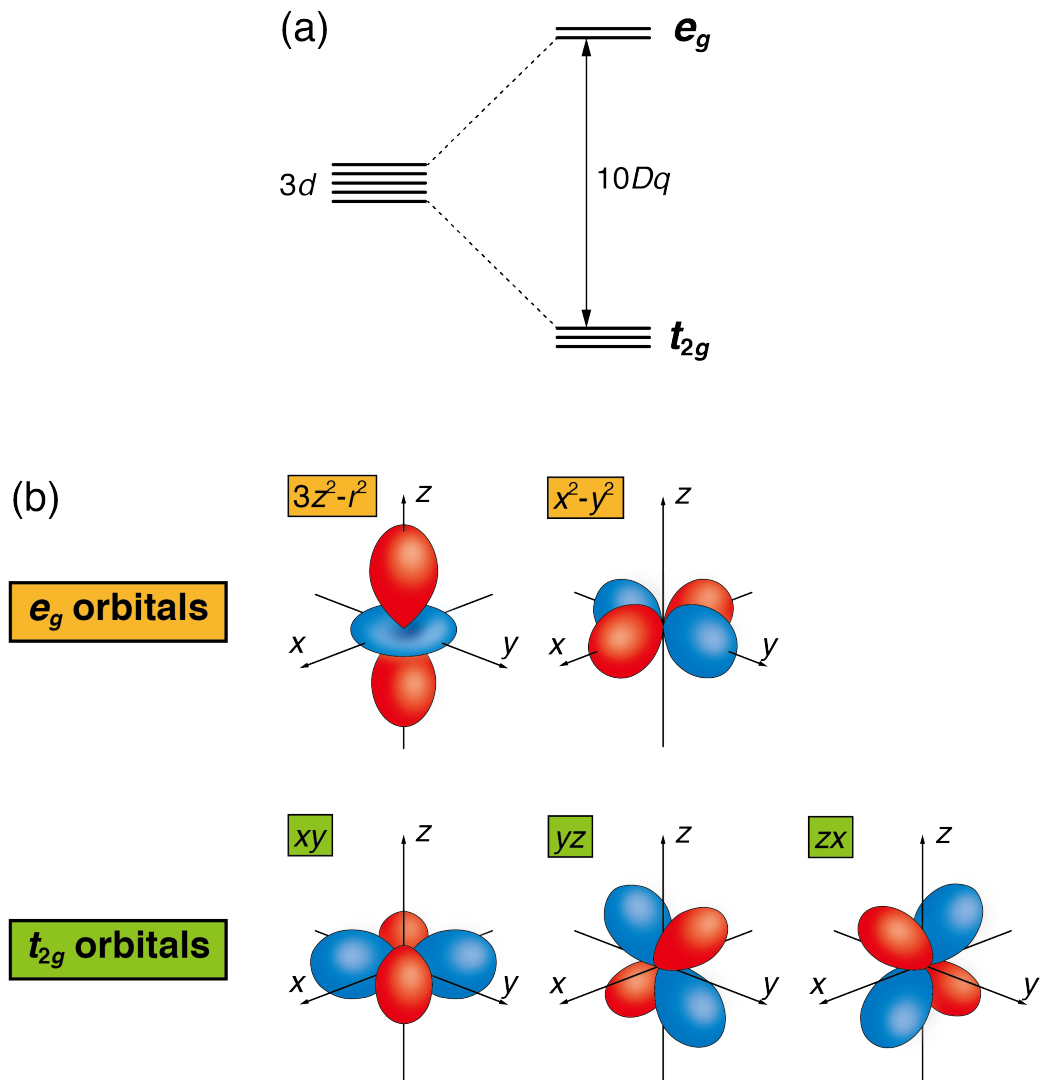
Figure 1-2. **(a)** Crystal-field splitting of $3d$ electronic state under O_h symmetry. **(b)** The schematics of $3d\_t_{2g}$ electron clouds (xy, yz, zx) and $3d\_e_g$ electron clouds ($3z^2-r^2$, x^2-y^2).

1.1.2. Quantum Paraelectricity

Both $SrTiO_3$ and $KTaO_3$ have the perovskite structure. Hence, they are known as typical quantum paraelectric (QPE) materials. [8, 9, 10] Generally, dielectric materials show ferroelectricity below a certain phase transition temperature called the Curie temperature (T_C). In case of $SrTiO_3$, the structural phase transition temperature is 105 K, which is comparatively lower than that of ferroelectric materials. Therefore, the paraelectric state remains, since quantum fluctuations suppress the ferroelectric state.

As shown in **Figure 1-3(a)**, the dielectric constant (ε_r) of $SrTiO_3$ (STO16) is gradually saturated without ferroelectric-like transition below 40 K. [11, 12] In the high temperature region, the temperature dependence of the dielectric constant shows the classical Curie-Weiss behavior. On the other hand, in the low temperature region, the graph is fitted using the Barrett-type quantum paraelectric law,

$$\varepsilon = \frac{A}{\dfrac{T_1}{2} \coth \dfrac{T_1}{2T} - T_C} \tag{1-1}$$

where A is a constant and T_1 is determined experimentally. [8] According to **Equation 1-1**, the relation between the dielectric constant and temperature is graphed in **Figure 1-3(b)**. In the low temperature region, the temperature dependence of the dielectric constant is well simulated using this equation.

(a)

(b)

$$a : T_C = -0.25T_1$$
$$b : T_C = 0$$
$$c : T_C = 0.25T_1$$
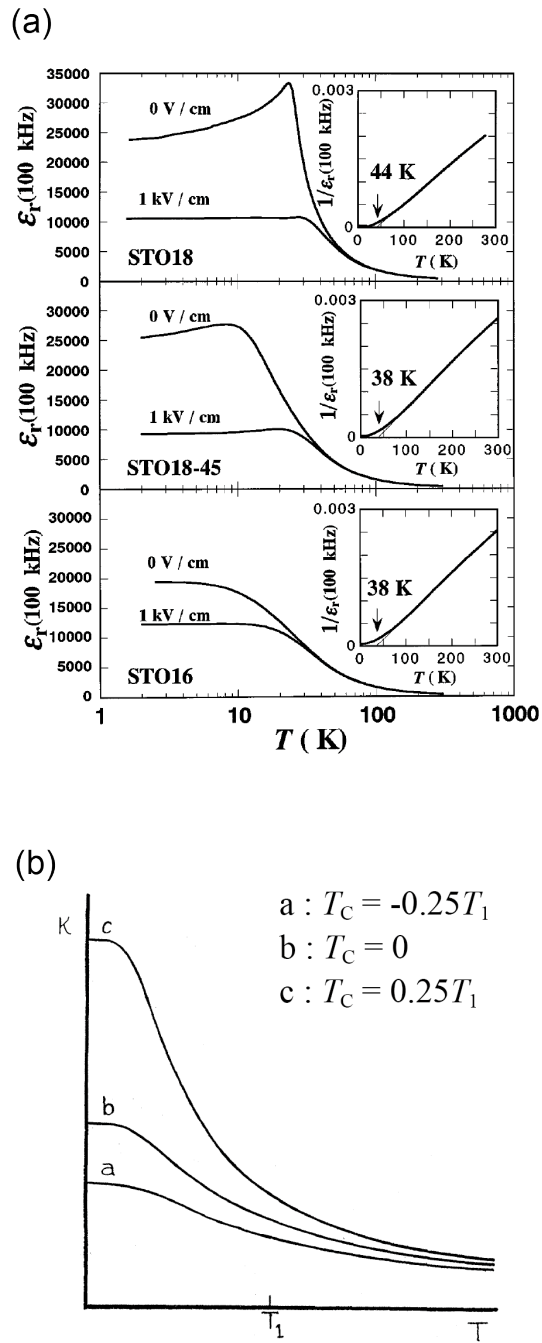
Figure 1-3. **(a)** Temperature dependence of the dielectric constant for $SrTiO_3$. [11] The bottom graph is for $SrTi^{16}O_3$ and the top graph is for $SrTi^{18}O_3$. **(b)** The dielectric constant as a function of temperature according to the Barrett-type quantum paraelectric law. [8]

1.1.3. Photoinduced Electric Dipole Moment

$SrTiO_3$ is known as a nearly ferroelectric material. This means that dielectric polarization easily arises owing to element substitution and external stimuli. For $SrTi^{16}O_3$, the oxygen isotopic exchange of ^{18}O induces ferroelectricity without the application of external fields. According to the measurements of the dielectric constants [see **Figure 1-3(a)**], the $SrTi^{18}O_3$ crystal shows ferroelectricity below 23 K. Homoepitaxial $SrTiO_3$ films with off-stoichiometry also lead to the ferroelectric phase transition at a temperature greater than room temperature. [13] Below 100 K, even stoichiometric $SrTiO_3$ shows enhancement of the dielectric constant under UV irradiation and if a bias direct-current (DC) electric field is applied, as shown in **Figure 1-4**. [14] This implies the existence of a polarized region under UV irradiation and a DC field at low temperature. The origin of the electric polarization induced by UV irradiation has been discussed by Hasegawa *et al*., [15] who proposed the presence of a photoinduced polar domain (PIPD) formed by lattice distortion. Photocarriers induced by UV excitation form polarons, [16] which distort the local symmetry around a Ti atom and lead to the formation of dipole moments. They suggested that the PIPD constructed by polarons induces anomalous dielectric behavior at low temperature.
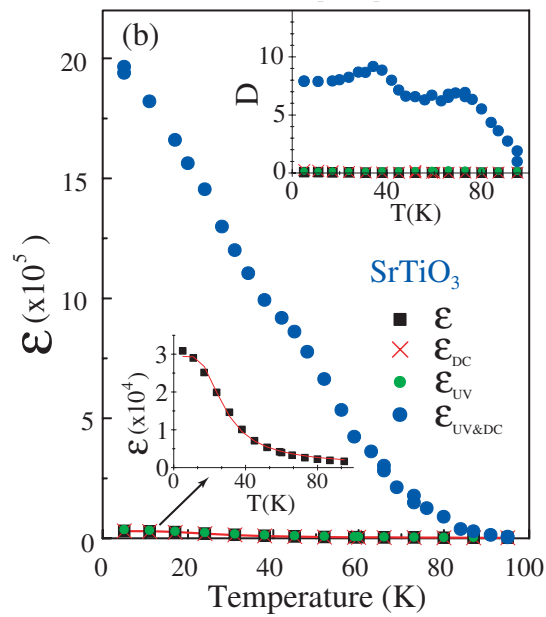
Figure 1-4. Temperature dependence of the dielectric constant of SrTiO$_3$. [14] Under UV irradiation and a DC field, the value of the dielectric constant ($\varepsilon_{UV\&DC}$) at 5 K is 60 times larger than the value of the dielectric constant without UV irradiation and DC field application (ε).
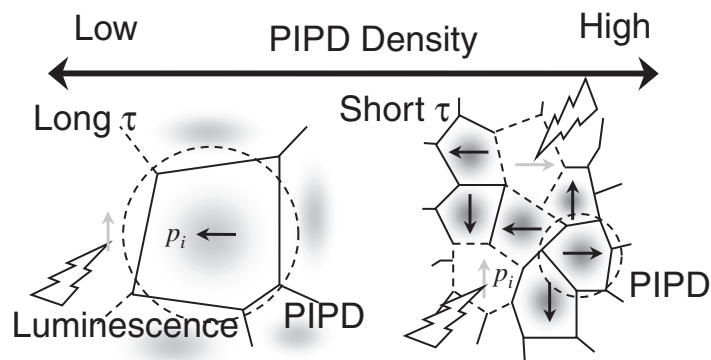
Figure 1-5. Schematic illustration of a photoinduced polar domain (PIPD). [15] Photocarriers induced by the interband excitation form small polarons, which distort the local symmetry around a Ti atom and lead to the formation of dipole moments.

These macroscopic physical phenomena induced by UV irradiaton have been studied through the research of the electronic structure. In this regard, Nozawa *et al.* investigated the temperature dependence and photoinduced change of Ti-$3d$ electronic states using X-ray absorption spectroscopy (XAS). [17] Using Ti K-edge XAS, the pre-peaks derived from t_{2g} and e_g components of Ti-$3d$ states are observed in the pre-edge region. The intensity decrease of these pre-peaks (A_1 and A_2) in **Figure 1-6(a)** shows that thermal-random vibration of a Ti atom is suppressed by cooling. In addition, the intensity of A_2 peak derived from e_g component increased under UV irradiation at low temperature, as shown in **Figure 1-6(b)**. The photoinduced enhancement of A_2 peak can be explained by uniaxial vibration of a Ti atom along the Ti–O bond direction. This result implies that the electric dipole moment is induced in the TiO_6 octahedron under UV irradiation.

The photoinduced electric dipole moment in quantum paraelectric $SrTiO_3$ is theoretically supported. The quantum fluctuation of perovskite oxides in the quantum paraelectric phase is influenced by T_{1u} phonons [**Figure 1-7(a)**] owing to the double-well potential along the Ti–O bond. [9, 18] In case of $SrTiO_3$ under UV irradiation, a photogenerated electron is weakly coupled with T_{1u} phonon (self-trapped off-center polaron). In addition, if an external electric field is applied, a photogenerated electron is trapped by multiple T_{1u} phonons aligned by the electric field as shown in **Figure 1-7(b)** (super-paraelectric large polaron). This large polaron has no long-range order. Therefore, it implies that the electric dipole moment and the local polar region are induced by UV irradiation.
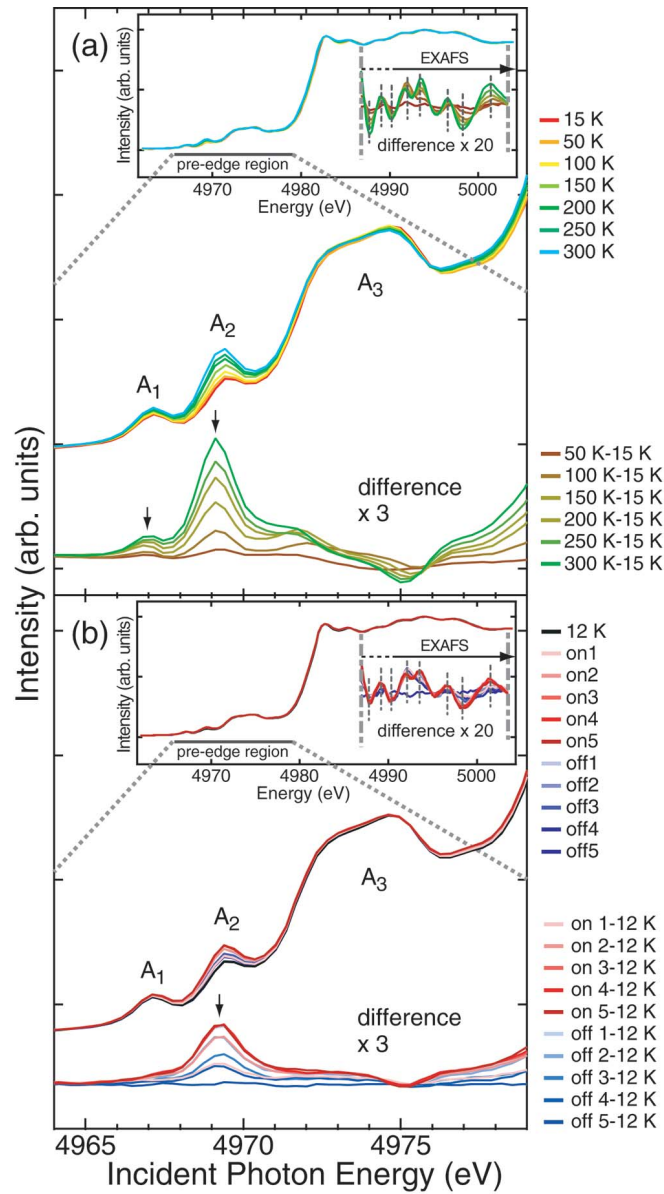
Figure 1-6. **(a)** Temperature dependence of the Ti *K*-edge XAS spectra in the pre-edge region of SrTiO$_3$. [17] **(b)** The photoinduced XAS spectra at 12 K. The lower lines in **(a)** and **(b)** show the difference spectra. A_1 and A_2 peaks are induced by a quadrupole (Ti $1s \rightarrow 3d$) transition. A_1 and A_2 peaks have the origin of t_{2g} and e_g components.
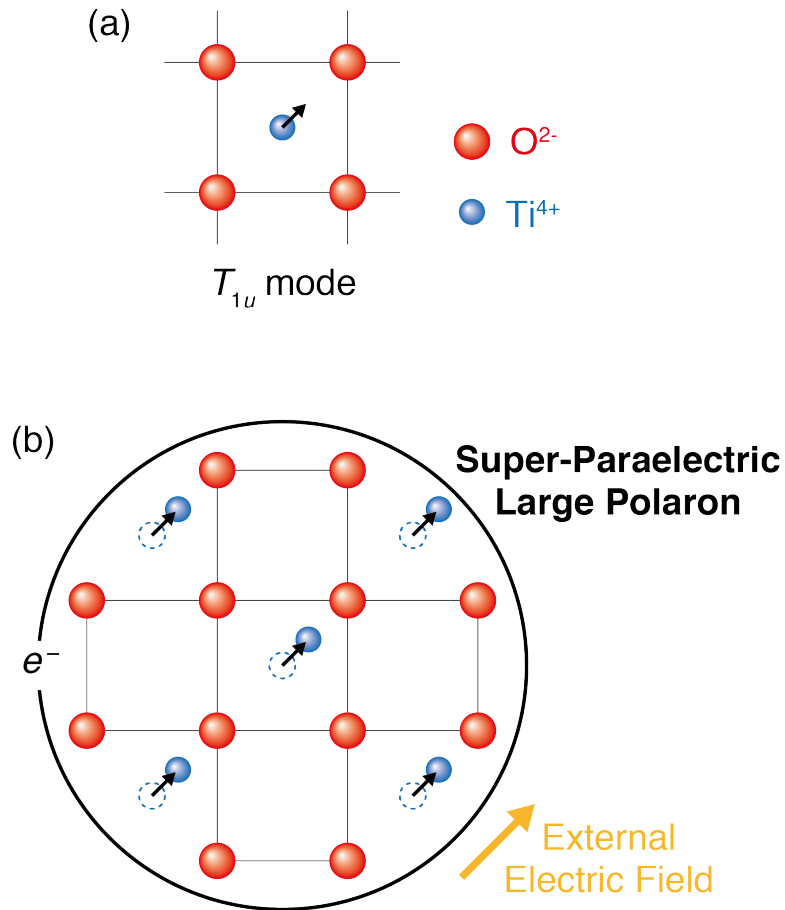
Figure 1-7. Schematic image of **(a)** T_{1u} mode and **(b)** a super-paraelectric large polaron. [18] A photogenerated electron is trapped by off-center polarons aligned by an external electric field.

A real-space image related to one-dimensional vibration was also obtained using high-resolution X-ray diffraction (XRD) and a maximum entropy method/Rietveld analysis. [19] **Figure 1-8** shows the difference electron-density distribution of Pr-doped $SrTiO_3$ obtained by subtracting "under UV data" from "without UV data." In **Figures 1-8(d)** and **1-8(e)**, the electron cloud around a Ti atom becomes elongated in the directions of the Ti–O bonds under UV irradiation at low temperature. The enhancement of the Ti–O bonds shows the one-dimensional vibration of the electron cloud around Ti atoms.
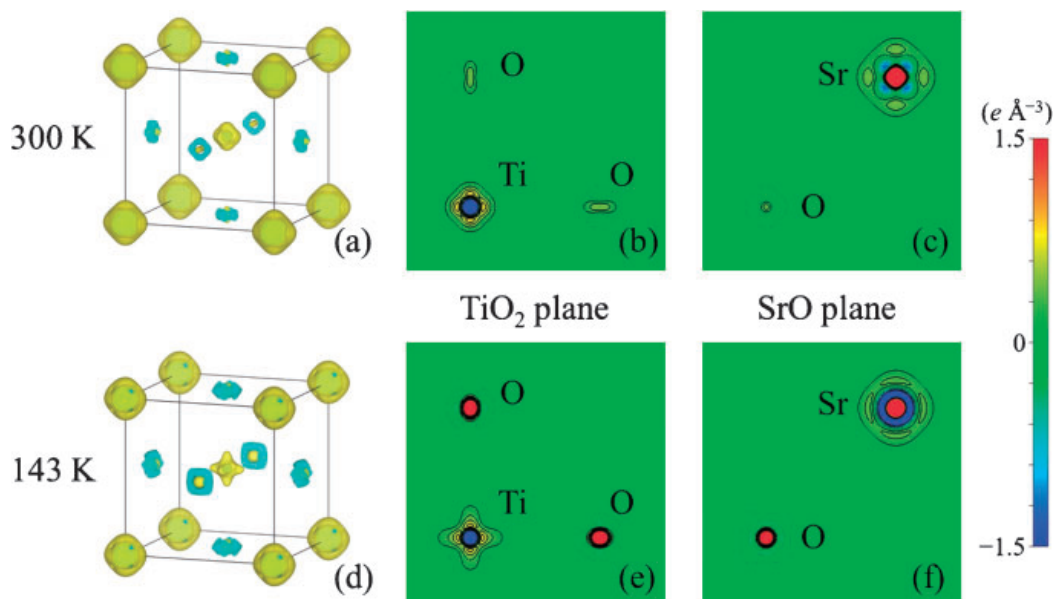
Figure 1-8. Difference electron density distribution of Pr-doped $SrTiO_3$ between "under UV" and "without UV". [19] Figures **(a)**–**(c)** are obtained at 300 K, figures **(d)**–**(f)** are obtained at 143 K. Figures **(a)** and **(d)** show the 3D contour maps. Figures **(b)** and **(e)** correspond to the cross-sections along the TiO_2 plane, and figures **(c)** and **(f)** correspond to the SrO plane.

1.2. Scope of This Study

1.2.1. Background

- **Local Origin of the PIPD**

Various photoinduced phenomena in $SrTiO_3$ have been studied by many researchers. In most cases, dielectric properties and their origins are discussed based on macroscopic measurements. Concerning dielectric measurements, PIPDs are believed to induce anomalous dielectric behavior at low temperature. It is also confirmed that UV light leads to distortion of the local symmetry around a Ti atom. However, in both cases the evidence of the atomic scale structure remains unclear. The microscopic origin of polar regions lies behind macroscopic behavior such as quantum fluctuations. In order to reveal anomalous dielectric behavior, the local structure around a Ti atom must be examined.

- **Advantage of Resonant X-ray Emission Spectroscopy**

Photoinduced one-dimensional vibration of a Ti atom along the Ti–O bond direction is demonstrated using Ti K-edge XAS measurements at low temperature. However, these results are inadequate for a definitive conclusion of the existence of the electric dipole moment, since there is no data on the electronic state of oxygen hybridized with Ti-$3d$ orbitals. Therefore, we perform Ti-$K\beta$ resonant X-ray emission spectroscopy (RXES) measurements, which provide the information about orbital hybridization and

low energy excitations along the Ti–O bond. The electric dipole moment is reveled in a unit cell directly.

1.2.2. Purposes of This Study

In this study, we investigate the origin of photoinduced Ti off-center displacement, i.e., the electric dipole moment in a unit cell. The purposes of this study are summarized below.

- **Electronic state observation**

For a $SrTiO_3$ single crystal in the QPE phase, the electronic state around a Ti atom is investigated using Ti-*L* and *K*β RXES measurements under external stimuli.

- **Ti off-center displacement**

In Ti-*K*β RXES measurements at low temperature, Ti off-center displacement is proved by the change of the charge transfer excitation.

- **Photoinduced polar region**

The local origin of the photoinduced polar region is revealed by the electronic state around a Ti atom.

Bibliography

[1] K. Ueno, S. Nakamura, H. Shimotani, A. Ohtomo, N. Kimura, T. Nojima, H. Aoki, Y. Iwasa, and M. Kawasaki, Nat. Mater. **7**, 855 (2008).

[2] S. Ohta, T. Nomura, H. Ohta, and K. Koumoto, J. Appl. Phys. **97**, 034106 (2005).

[3] A. F. Santander-Syro, O. Copie, T. Kondo, F. Fortuna, S. Pailhès, R. Weht, X. G. Qiu, F. Bertran, A. Nicolaou, A. Taleb-Ibrahimi, P. Le Fèvre, G. Herranz, M. Bibes, N. Reyren, Y. Apertet, P. Lecoeur, A. Barthélémy, and M. J. Rozenberg, Nature **469**, 189 (2011).

[4] W. Meevasana, P. D. C. King, R. H. He, S.-K. Mo, M. Hashimoto, A. Tamai, P. Songsiriritthigul, F. Baumberger, and Z.-X. Shen, Nat. Mater. **10**, 114 (2011).

[5] A. Ohtomo and H. Y. Hwang, Nature **427**, 423 (2004).

[6] D. Kan, T. Terashima, R. Kanda, A. Masuno, K. Tanaka, S. Chu, H. Kan, A. Ishizumi, Y. Kanemitsu, Y. Shimakawa, and M. Takano, Nat. Mater. **4**, 816 (2005).

[7] D. Kan, R. Kanda, Y. Kanemitsu, Y. Shimakawa, M. Takano, T. Terashima, and A. Ishizumi, Appl. Phys. Lett. **88**, 191916 (2006).

[8] J. H. Barrett, Phys. Rev. **86**, 118 (1952).

[9] K. A. Müller and H. Burkard, Phys. Rev. B **19**, 3593 (1979).

[10] J. Hemberger, M. Nicklas, R. Viana, P. Lunkenheimer, A. Loidl, and R.Böhmer, J. Phys.: Condens. Matter **8**, 4673 (1996).

[11] M. Itoh, R. Wang, Y. Inaguma, T. Yamaguchi, Y.-J. Shan, and T. Nakamura, Phys. Rev. Lett. **82**, 3540 (1999).

[12] M. Itoh and R. Wang, Appl. Phys. Lett. **76**, 221 (2000).

[13] D. A. Tenne, A. K. Farrar, C. M. Brooks, T. Heeg, J. Schubert, H. W. Jang, C. W. Bark, C. M. Folkman, C. B. Eom, and D. G. Schlom, Appl. Phys. Lett. **97**, 142901

(2010).

[14] M. Takesada, T. Yagi, M. Itoh, and S. Koshihara, J. Phys. Soc. Jpn. **72**, 37 (2003).

[15] T. Hasegawa, S. Mouri, Y. Yamada, and K. Tanaka, J. Phys. Soc. Jpn. **72**, 41 (2003).

[16] T. Hasegawa, M. Shirai and K. Tanaka, J. Lumin. **87**–**89**, 1217 (2000).

[17] S. Nozawa, T. Iwazumi, and H. Osawa, Phys. Rev. B **72**, 121101(R) (2005).

[18] K. Nasu, Phys. Rev. B **67**, 174111 (2003)

[19] N. Nakajima, M. Deguchi, H. Maruyama, H. Osawa, C. Moriyoshi, and Y. Kuroiwa, Jpn. J. Appl. Phys. **52**, 09KF05 (2013).

2. Experimental Methods

2.1. X-ray Spectroscopy

X-rays are electromagnetic waves with short wavelengths from 10^{-11} to 10^{-8} nm. Their energy range is from 100 eV to 100 keV. Electromagnetic waves with various energies have specific properties and lose energy because of some interactions with nuclei and electrons in materials. This phenomenon is referred as "absorption." As shown in **Figure 2-1**, various processes, such as character X-ray emission, elastic and inelastic scattering, and photoelectron emission, occur while X-ray absorption. The probability of each process varies depending on the irradiated material and the incident X-ray energy. In this study, we used X-ray absorption spectroscopy (XAS) and X-ray emission spectroscopy (XES) to detect inelastic scattering and fluorescence X-rays.
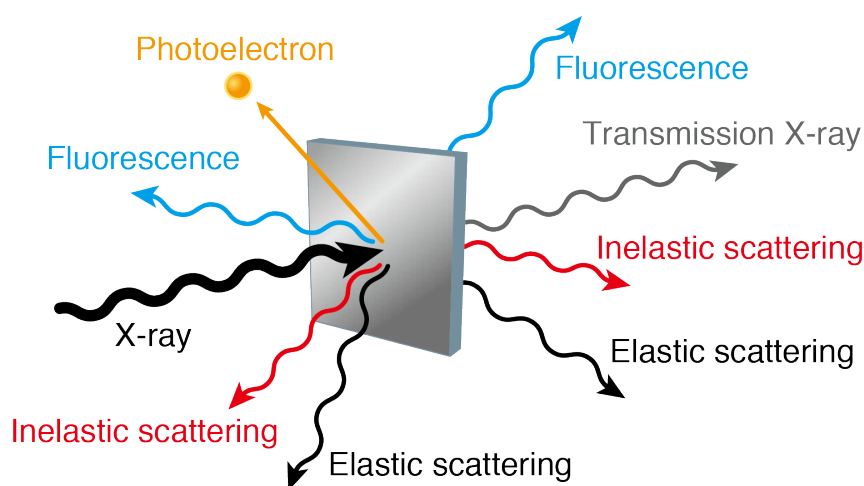
Figure 2-1. Interaction between an X-ray and a material. When the X-ray irradiates the material, photons and electrons with various energies are emitted.

2.1.1. X-ray Absorption Spectroscopy

An electron is excited from the ground state to an unoccupied state of valence or conduction band when an X-ray is absorbed. The experimental method for measuring the energy dependence of X-ray absorption coefficient μ is called XAS. We can get the information mainly about electronic states of absorbing atoms and local structures around absorbing atoms. The transition probability of an electron irradiated by an X-ray is obtained using Fermi's golden rule.

The left side of **Figure 2-2** is the schematic diagram of the XAS spectrum. Several jumps in the absorption coefficient corresponding to the absorption edges can be observed. The *K*-edge XAS spectrum is divided into two regions: X-ray absorption near-edge structure (XANES) and extended X-ray absorption fine structure (EXAFS). The electronic state and coordination environment of an absorbing atom are reflected in the XANES region. EXAFS, the higher energy side of the edge jump is a broad oscillating structure resulting from interference between a photoelectron and the scattering wave formed by scattering of the photoelectron by neighboring atoms. The local structure around an X-ray absorbing atom is obtained through radial distribution functions using the Fourier transformation of oscillating components in the EXAFS region.

The absorption edge energy corresponds to the energy of excitation between quantized electronic states. The excitation energy differs depending on the element. For this reason, electron transition is selectively observed by tuning to a specific energy even if a target material is composed of multiple elements.

Absorption coefficient μ is directly observed using transmission measurements. In this method, a XAS spectrum is expressed by

$$\mu t = \ln \frac{I_0}{I} \tag{2-1}$$

where I_0 is the incident X-ray intensity, I is the transmitted X-ray intensity, and t is the sample thickness. The sample should be thin enough for penetrating X-rays with a certain intensity. Although the transmission method is an easily-performed measurement technique, this method is not adequate for thick samples like single crystals.

A XAS spectrum can be also observed by detecting fluorescence. Excited electrons and holes created by the X-ray absorption process are relaxed owing to emission of fluorescence X-rays and Auger electrons. The yield of fluorescence X-rays and Auger electrons are proportional to the X-ray absorption coefficient. Therefore, we can indirectly observe the absorption coefficient by detecting them (**Figure 2-3**). The fluorescence method has two options. One option is a total fluorescence yield (TFY) mode, in which all fluorescence X-rays are detected regardless of their energy. Another option is a partial fluorescence yield (PFY) mode, in which the fluorescence X-ray energy is measured, and then the fluorescence X-rays with a specific energy are monitored.
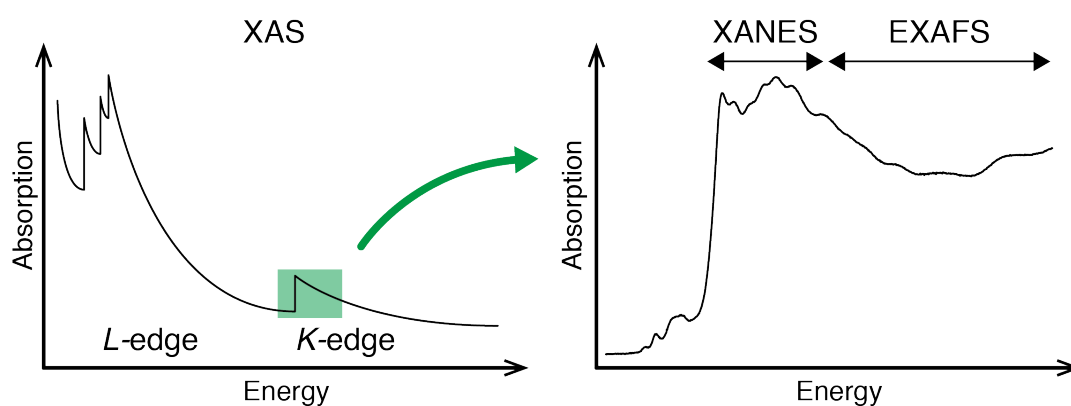
Figure 2-2. Schematic of X-ray absorption as a function of the incident photon energy. The right figure is the Ti *K*-edge XAS spectrum as an example.
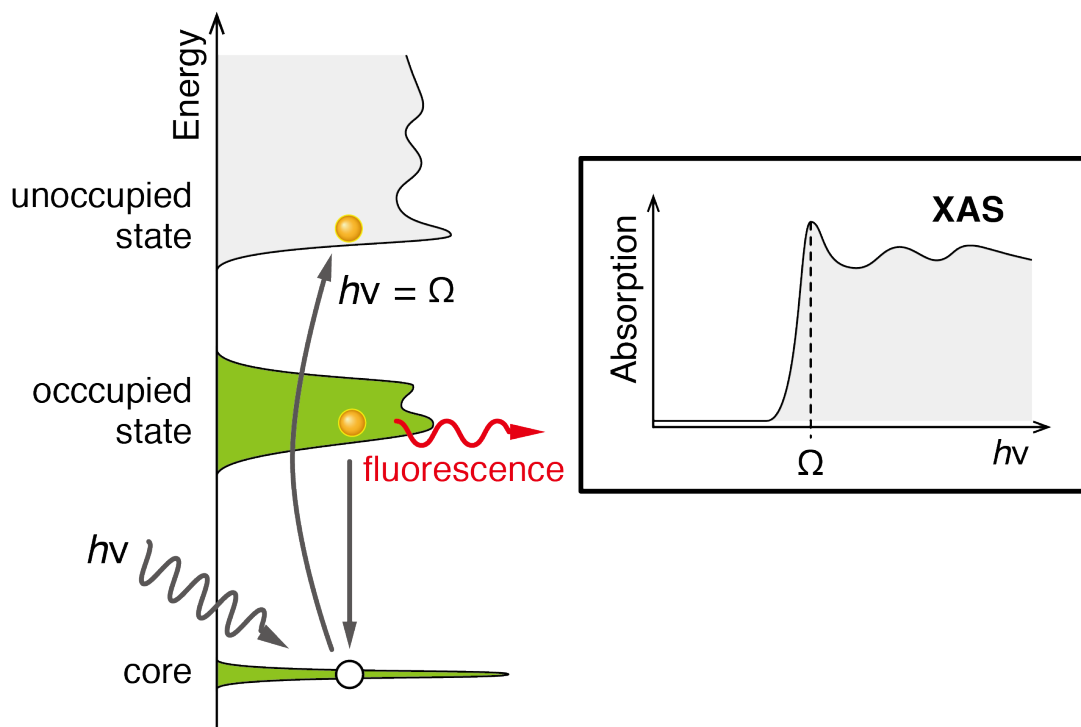
Figure 2-3. Schematic XAS diagram of the fluorescence method. In the PFY mode, the fluorescence X-rays with a specific energy are detected as functions of the incident X-ray energy.

2.1.2. X-ray Emission Spectroscopy

When a core hole is created by an X-ray, the outer-shell electron immediately occupies the hole through various relaxation channels emitting excess energy as a fluorescence X-ray or exciting other electrons as Auger electrons, as shown in **Figure 2-4(a)**. The used spectroscopic method for detecting emitted X-rays in the second-order optical process is XES. The intensity of the XES signal is significantly weaker than that of the first-order optical process such as X-ray absorption and photoelectron emission. However, XES has several advantages. Since XES is a photon-in/photon-out technique,

the measurements can be performed under external fields, e.g., magnetic and electric fields, which cannot be used if electron-detection methods are implemented. XES is insensitive to the charge-up phenomena. Thus, it can be used not only for metals but also for insulators. The XES optical process follows a clear selection rule due to the core-hole localization. Therefore, the localized density of states and electronic structures around specific atoms can be observed. For researches on complex compounds and strongly-correlated electron systems, XES is still a suitable experimental approach.

2.1.3. Resonant X-ray Emission Spectroscopy

In a normal XES process, an incident X-ray has sufficiently high energy compared to the electron-binding energy, and core electrons are excited to higher energy bands above the Fermi level. Then the fluorescence X-rays with a constant emission energy are observed regardless of the incident X-ray energy. Two first-order optical processes, excitation and relaxation, occur successively. On the other hand, RXES exciting to near absorption edge depends on the incident X-ray energy. When the ground electrons are selectively excited to a specific intermediate state, the emission spectra consist of not only fluorescence X-rays but also X-rays scattered inelastically owing to the Raman scattering [**Figure 2-4(b)**]. The Raman scattering occurs if the incident (excitation) X-ray energy is close to the energy difference between the ground state and an unoccupied state (resonance condition). The resonance effect becomes clear if the unoccupied state is localized with a narrow energy width. X-ray Raman scattering provides the information on electronic states. The Raman peaks in RXES spectra are mainly influenced by orbital hybridization between constituent elements and reflect low-energy excitations in materials. The excitations induced by the crystal field and charge transfer are described in the following subsection.

A RXES spectrum is expressed by the Kramers-Heisenberg formula as follows:

$$F(\Omega, \omega) = \sum_f \left| \sum_m \frac{\langle f | T_2 | m \rangle \langle m | T_1 | i \rangle}{E_i - E_m + \Omega - i\Gamma} \right|^2 \times \delta(E_i - E_f + \Omega - \omega) \tag{2-2}$$

where Ω and ω are the incident and emitted photon energies, respectively, $|i\rangle$, $|m\rangle$, and $|f\rangle$ are the initial, intermediate, and final states, respectively, E_i, E_m, and E_f are the energies of each state, respectively, Γ is the spectral broadening due to the core-hole lifetime in the intermediate state, and T_1 and T_2 are the dipole transition operators.
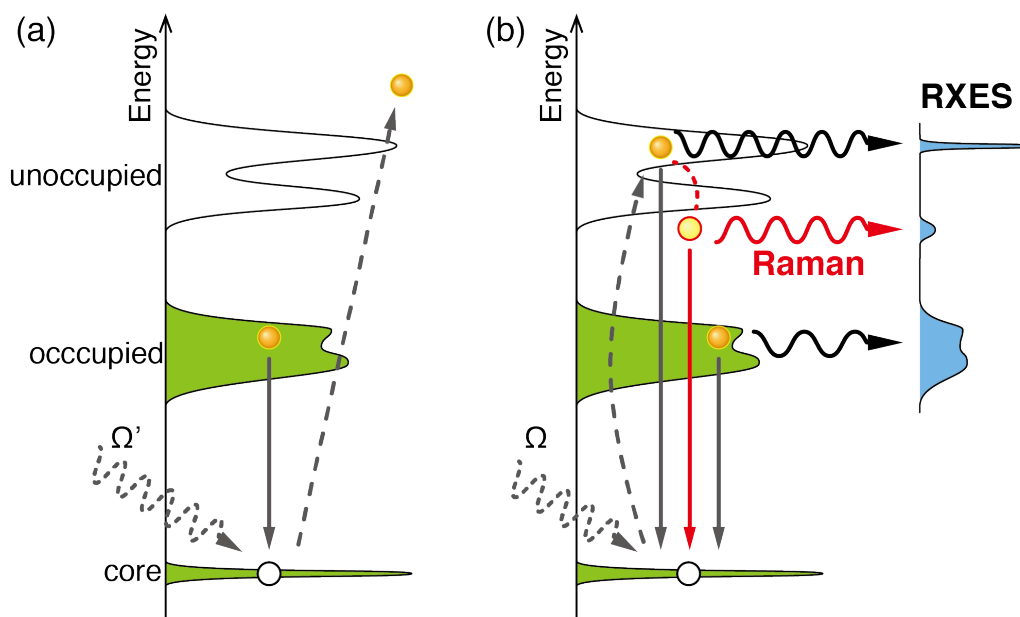
Figure 2-4. Schematic model of the optical processes when **(a)** XES and **(b)** RXES are used. The resonance excitation provides information on orbital hybridization and low-energy excitation in materials.

- **Crystal Field Excitation**

$3d$ states in a $3d$ transition metal under O_h symmetry are split into t_{2g} and e_g states by the crystal field. We concentrate on the explanation of titanates. A titanate, such as TiO_2 and $SrTiO_3$, has nominally no $3d$ electron from the viewpoint of ionic bonding. After a slight perturbation or defects, a part of $3d$ orbitals is occupied by electrons. The initial state of one $3d$ electron system is represented as $2p^6 3d^1\_t_{2g}$ via p–d hybridization between O-$2p$ and Ti-$3d$ orbitals. When a Ti-$2p$ electron is resonantly excited to Ti-$3d\_e_g$ state ($2p^5 3d^1\_t_{2g} 3d^1\_e_g$), there exists two final states exist: $2p^6 3d^1\_t_{2g}$ and $2p^6 3d^1\_e_g$. Compared with the initial state, the final $2p^6 3d^1\_e_g$ state seems to be generated through the dipole-forbidden transition from $3d\_t_{2g}$ to $3d\_e_g$ as shown in **Figure 2-5**. In the Kramers-Heisenberg formula (**Equation 2-1**), the intermediate states are included as a unit operator $\sum_m |m\rangle\langle m| = 1$. Hence, the dipole-forbidden transition seems to be possible. This apparent transition is referred to as crystal field excitation or *dd* excitation. In a RXES spectrum, the *dd* excitation peak is located close to the elastic peak. Without a *d* electron, no *dd* excitation peak is observed in the d^0 electronic configuration. *dd* peak is a good demonstration of *d* electrons in d^0 systems.
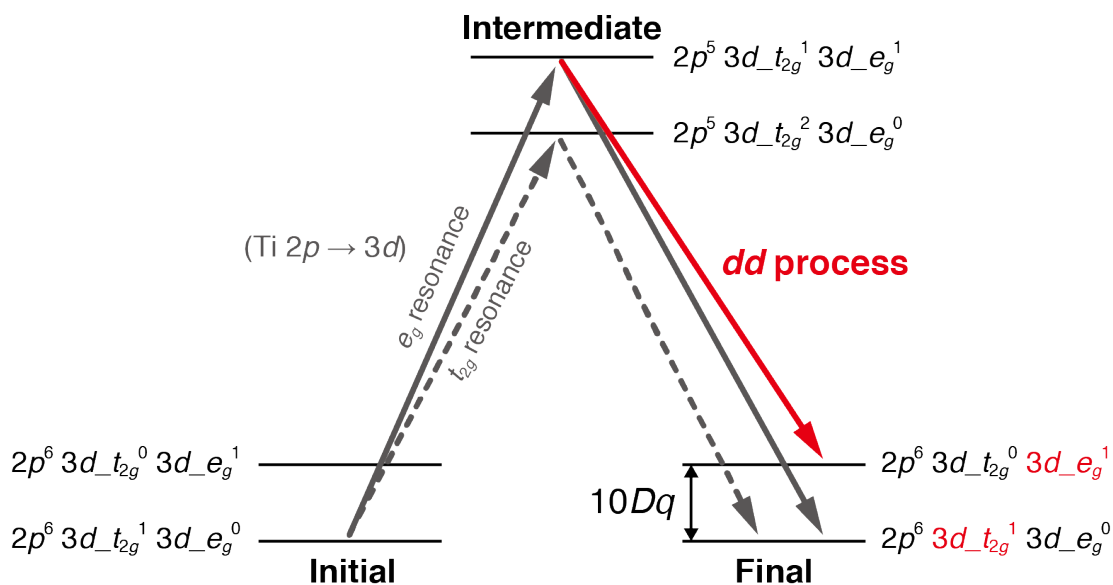
Figure 2-5. Schematic RXES energy-level diagram of crystal-field excitation. The red arrow corresponds to the *dd* process.

- **Charge Transfer Excitation**

The Ti^{4+} ion in $SrTiO_3$ is surrounded by the nearest six-neighbor O^{2-} ions. The valence electronic configuration is $3d^0$ in the unperturbed ground state. However, an electron-doped state is also introduced by oxygen vacancy creation and local distortion of the crystal lattice. Then $d^1\underline{L}$ state with charge transfer (CT) from an oxygen atom is created and couples with $3d^0$ state via hybridization interaction, where $\underline{L}$ represents a ligand (oxygen) hole.

Figure 2-6 is the schematic RXES energy-level diagram of the charge-transfer process in $SrTiO_3$. The final state matches initial state $c3d^04p^0$ in most cases. This process is observed as elastic scattering in a RXES spectrum. In addition, another process occurs when some final states become $c3d^14p^0\underline{L}$ mediated by charge-transfer

excitation between Ti-3d and O-2p orbitals. The charge-transfer process requires a little energy (the charge-transfer energy: Δ). Therefore, the CT peak appears on the lower energy side of the elastic peak with an energy separation of Δ.
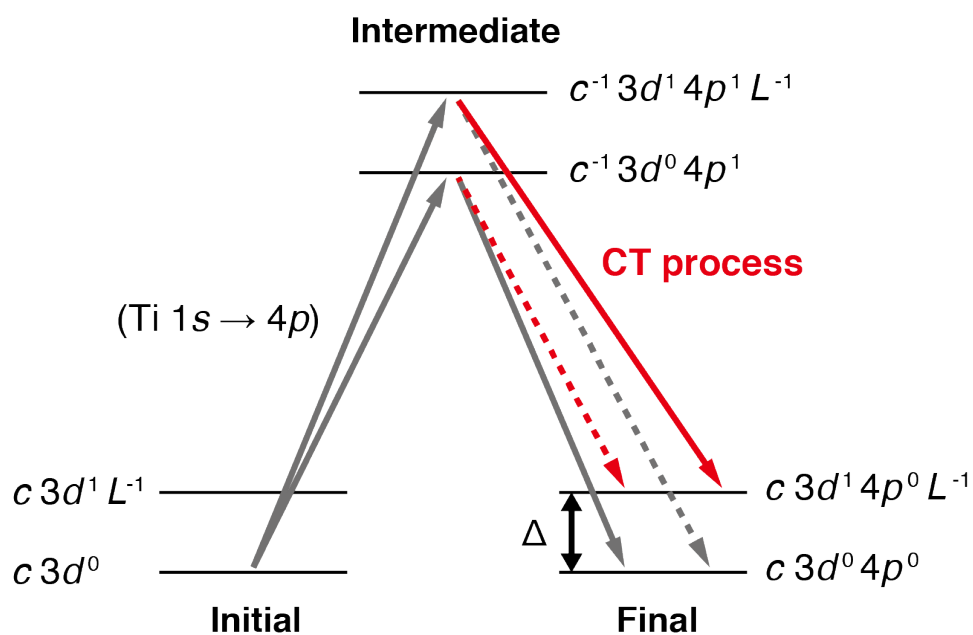
Figure 2-6. Schematic RXES energy-level diagram of the charge-transfer process. c ($\underline{c}$) represents a core electron (hole).

2.2. Synchrotron Radiation

2.2.1. Photon Factory at Institute of Materials Structure Science

- **Undulator Beamline BL-2C**

The Photon Factory (PF) is the second-generation synchrotron radiation source facility in the High Energy Accelerator Research Organization (KEK), Japan. [1] The PF ring storing 2.5 GeV electron beam supplies X-rays and vacuum-ultraviolet light, which is used in a wide range of fields from material science to biological science.

Ti L-edge XAS and RXES measurements were performed at the undulator beamline, BL-2C, whose schematic view is shown in **Figure 2-7** [2]. A varied-line-spacing plane grating with an average groove density of 1000 lines/mm was used to monochromatize a soft x-ray beam (250 ~ 1400 eV). A soft x-ray emission spectrometer is installed on the front end of this beamline, which can measure Ti-L emission spectra in vacuum. [3] This instrument is consisted of two-dimensional detector, gratings, photoelectron energy analyzer, and sample bank. The X-ray emission spectrometer shown in **Figure 2-8** is structured on the basis of a Rowland mount type. Hence, the slit and the grating are fixed, and the two-dimensional detector moves in the Roland circle. The translation of the two-dimensional detector is triaxially controlled by a computer. Peripheral aberration is induced outside the center of the detector plane placed on the Rowland circle. However, detected image correction with consideration of the aberration can avoid spectral resolution deterioration. A closed-cycle helium cryostat mounted on this spectrometer enables us to perform low-temperature measurements. UV light emitted from a He-Cd laser (Kimmon-Koha IK 5451R-E) with wavelength of 325 nm is introduced through a quartz glass port.
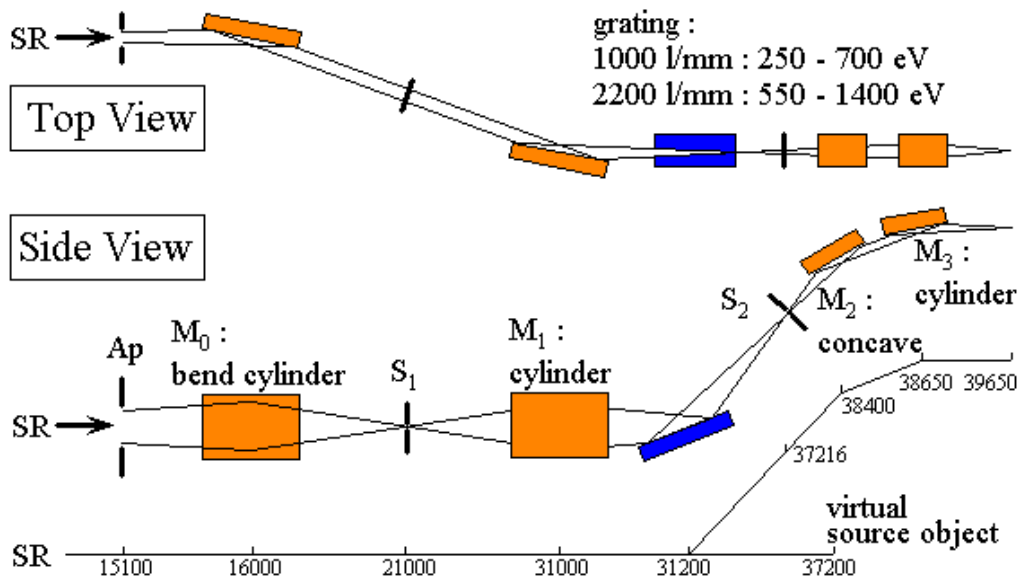
Figure 2-7. Beamline layout of BL-2C at the PF. [2]

Table 2-1. X-ray specification in BL-2C at PF. [2]

Energy range	$250 \sim 1400$ eV
Photon flux	$10^9 \sim 10^{10}$ photons/sec/0.02%BW
Energy resolution	$\Delta E/E \sim 1 \times 10^{-4}$
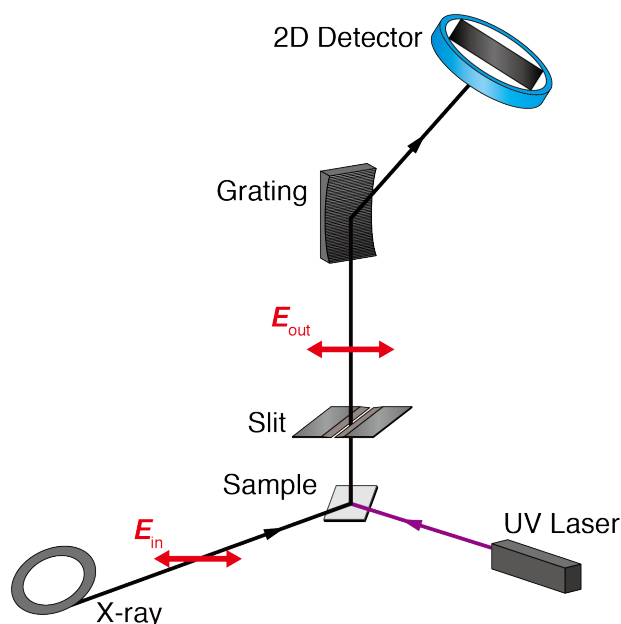
Figure 2-8. Schematic view of the experimental system of BL-2C at the PF. This instrument can measure Ti-*L* emission spectra in vacuum.

2.2.2. Synchrotron Radiation Facility SPring-8

• Undulator Beamline BL39XU

SPring-8 is a large synchrotron radiation facility in Japan and stores electron beams with energies of 8 GeV. [4] SPring-8 that is the third generation light source opens many undulator beamlines with powerful beams to scientists worldwide. Using ultra-bright and quasi-monochromatic light emitted from an undulator, energy, angle, and time resolutions can be improved significantly. A bending-magnet light source and a wiggler are also installed. Therefore, synchrotron radiation from hard X-ray region (300 keV) to soft X-ray region (170 eV) is available.

Ti *K*-edge XAS and Ti-*K*β RXES measurements were performed at undulator beamline BL39XU, which provides X-rays with various polarization states. The schematic view is shown in **Figure 2-9**, and characteristics of the X-rays at the sample position are listed in **Table 2-2**. [5] The X-rays delivered from a liner undulator in vacuum are monochromatized using a diamond (111) double-crystal monochromator. A mechanically bended mirror provides a horizontally focused beam (50 ~ 100 μm in full width at half maximum). Moreover, an extra focused beam of 8 μm (V) × 7 μm (H) is formed by a Kirkpatrick and Baez (KB) mirror installed in front of the sample. A movable diamond X-ray phase retarder (XPR) is installed between the monochromator and the mirror. A 0.1-mm-thick XPR incorporated under the half-wave plate condition easily changes the X-ray polarization state from horizontal to vertical.

The setup of Ti *K*-edge XAS and Ti-*K*β RXES measurements is schematically depicted in **Figure 2-10**. The XAS spectra were measured using the fluorescence-yield method through a silicon drift detector (SDD). In the RXES measurements, the emitted X-rays were monochromatized using a Ge(331) analyzer crystal with a spherical curvature and subsequently detected using PILATUS two-dimensional detector. [6] The X-ray paths were filled with helium gas to prevent scattering of X-rays by air.
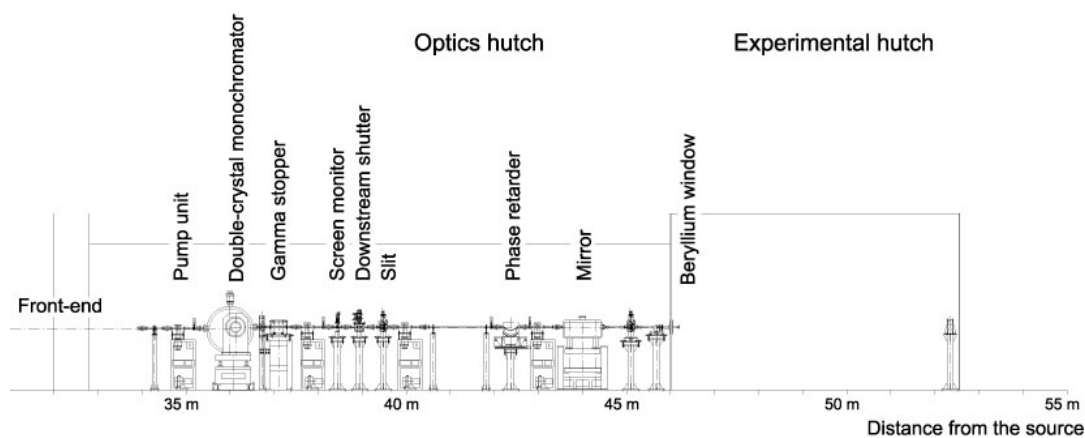
Figure 2-9. Beamline layout of BL39XU at SPring-8. [5]

Table 2-2. X-ray specifications in BL39XU at SPring-8. [5]

Energy range	5 ~ 38 keV (Si 111), 5 ~ 61 keV (Si 220)
Flux at sample	5.3×10^{13} photons/sec (Si 111), 2.4×10^{13} photons/sec (Si 220)
Energy resolution	$\Delta E/E \sim 2 \times 10^{-4}$ (Si 111), $\Delta E/E \sim 1 \times 10^{-4}$ (Si 220)
Linear polarization rate	99.9%
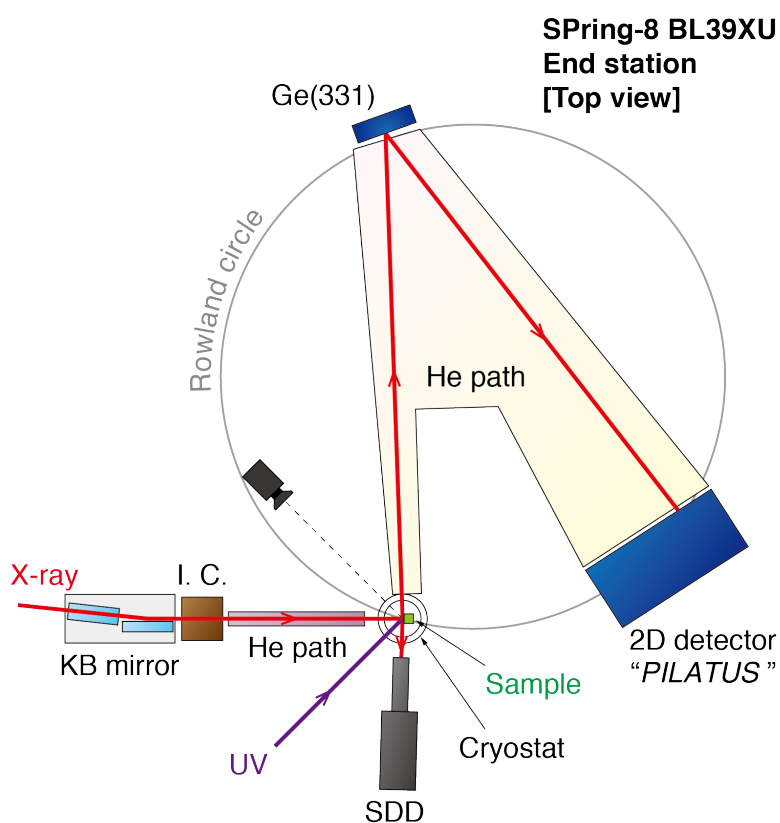
Figure 2-10. Schematic view of the experimental system of the end station of BL39XU at SPring-8. RXES and XAS measurements are performed using the micro-focus X-ray beam formed by the KB mirror. The X-ray paths are filled with helium gas to prevent scattering of X-rays by air.

2.3. Sample Preparation

The sample used in this study was a $SrTiO_3$ single crystal with a purity of 99.99% purchased from Crystal Base. In Ti L and K-edge measurements, the sample was attached to a beryllium-copper holder using grease with high thermal conductivity. **Figure 2-11** shows the photograph of the sample folder for Ti K-edge X-ray spectroscopic measurements under UV irradiation and a DC field at low temperature. Silver-paste electrodes were attached to one side with a 0.5 mm separation for applying a DC field in the [001] direction. UV light and X-rays were focused onto the same point between the electrodes. For applying a DC field, Au wires with diameters of 0.1-mm were used to suppress thermal leak into the sample. A sapphire plate was used to isolate the sample from the holder electrically and thermally.

Our own sample holder system attached to the existing closed-cycle helium cryostat is constructed to perform low-temperature Ti-$K\beta$ RXES measurements under UV irradiation and a DC field. This system is consisted of a sample holder attached to the cold head of the cryostat, radiation shield to block thermal radiation, and shroud to evacuate air, as shown in **Figure 2-13**. The sample holder and the radiation shield are made of Cu to provide high thermal conductivity. The radiation shield and the shroud have five windows for incoming X-ray, emission, UV-light, and sample monitoring at the same level as the incident X-ray level. In particular, the windows of the shroud for incident X-rays, emitted X-rays, and UV light are covered using a Be plate, polyimide film, and quartz glass, respectively. A UV-light beam guided by an optical fiber was focused onto the X-ray spot on the sample with a flux power of $4\,mW/cm^2$. This cryostat has vacuum feed-through for conducting wires to apply an electric field. Therefore, this sample holder system enables us to perform RXES measurements under UV irradiation and a DC field at low temperature.
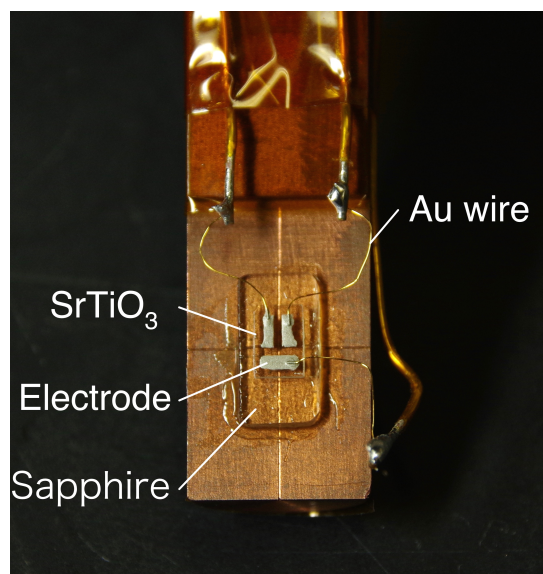
Figure 2-11. Sample holder for Ti *K*-edge X-ray spectroscopic measurements under UV irradiation and a DC field at low temperature. $SrTiO_3$ and a sapphire plate are attached using grease.
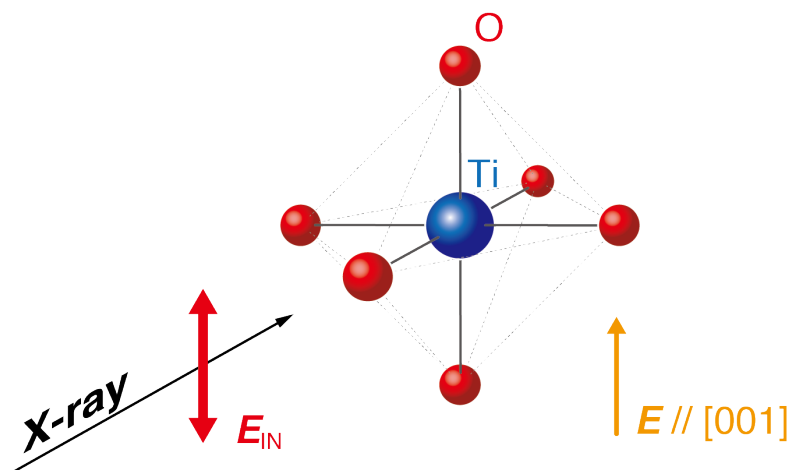
Figure 2-12. Relation between the directions of X-ray polarization, DC field (***E***), and Ti–O bond. The polarization vector of incident X-rays is parallel to the [001] direction, which also corresponds to the Ti–O bond. The DC field is also applied in the direction of the X-ray polarization.

Emitted X-ray

Holder

Radiation shield

Shroud

Monitoring

Emitted X-ray

Incident X-ray

UV

Enlarged view around sample

Sample

Sapphire

Electrode

Au wire
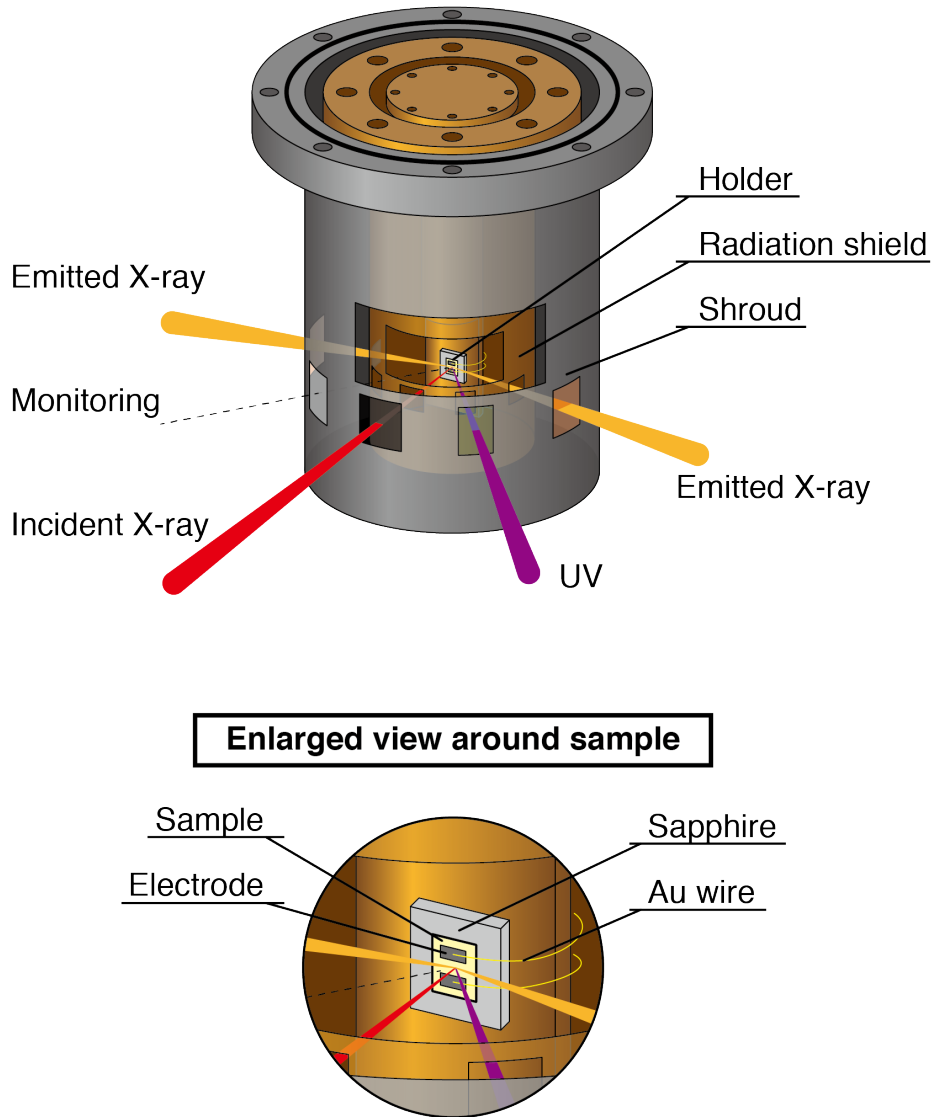
Figure 2-13. Schematic view of the sample holder system for low-temperature measurements under UV irradiation and a DC field. The bottom illustration shows the enlarged view around sample.

Bibliography

[1]   Photon Factory, http://www2.kek.jp/imss/pf/eng/

[2]   Photon Factory, BL-2C,
      http://pfwww.kek.jp/users_info/station_spec/bl2/bl2c.html

[3]   Y. Harada, H. Ishii, M. Fujisawa, Y. Tezuka, S. Shin, M. Watanabe, Y. Kitajima,
      and A. Yagishita: J. Synchrotron Radiat. **5**, 1013 (1998).

[4]   SPring-8, http://www.spring8.or.jp/en/

[5]   SPring-8, BL39XU,
      http://www.spring8.or.jp/wkg/BL39XU/instrument/lang-en/INS-0000000312/instrument_summary_view

[6]   H. Toyokawa, Ch. Broennimann, E. F. Eikenberry, B. Henrich, M. Kawase, M. Kobas, P. Kraft, M. Sato, B. Schmitt, M. Suzuki, H. Tanida, and T. Uruga, Nucl. Instrum. Methods Phys. Res., Sect. A **623**, 204 (2010).

3. Results and Discussion

3.1. Ti *L*-edge XAS and RXES Measurements

3.1.1. Ti *L*-edge XAS Measurements

The Ti *L*-edge XAS spectrum of a $SrTiO_3$ single crystal at 40 K is composed of four major peaks (**Figure 3-1**). As shown in **Figure 3-2**, Ti-2*p* states are split into L_2 and L_3 due to spin-orbital interaction, and Ti-3*d* states are split into t_{2g} and e_g due to crystal field splitting. Since absorption occurs between these states, the major peaks labeled as *a*, *e*, *i*, and *k* correspond to the absorption of Ti-$2p_{3/2}$ (L_3) $\rightarrow$ $3d\_t_{2g}$, $3d\_e_g$ and Ti-$2p_{1/2}$ (L_2) $\rightarrow$ $3d\_t_{2g}$, $3d\_e_g$ in the order from lower to higher incident energies. The two broad features (S_1 and S_2) above the major peaks are satellites of the charge transfer between Ti and O. [1, 2] The pre-peaks denoted as *P* are observed below the first major peaks, but their origin is unclear.

3.1.2. Ti-*L* RXES Measurements

Figure 3-3 shows the Ti-*L* RXES spectrum of stoichiometric $SrTiO_3$ at 40 K. The excitation energy equaled the Ti $L_{3\_e_g}$ absorption-edge energy labeled as *e* in **Figure 3-1**. The energy difference from the elastic peak is denoted as the transferred energy (E_{Tr}). There are broad $L\alpha_{1,2}$ fluorescence peak and two characteristic features on both sides of $L\alpha_{1,2}$. A peak at $E_{Tr} = 12$ eV and a shoulder at 5 eV are defined as *A* and *B*, respectively.
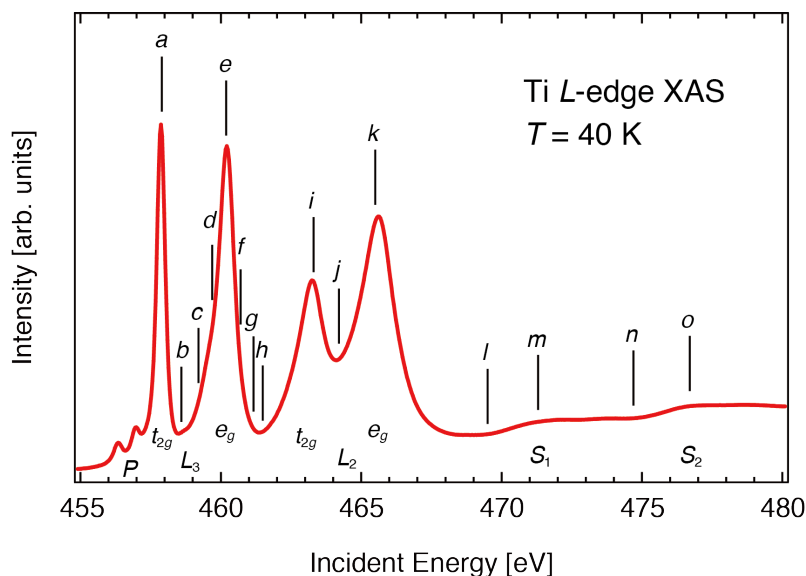
Figure 3-1. Ti *L*-edge XAS spectrum of a SrTiO$_3$ single crystal at 40 K. The vertical bars with characters (*a–o*) represent the excitation energies of the Ti-*L* RXES measurements.
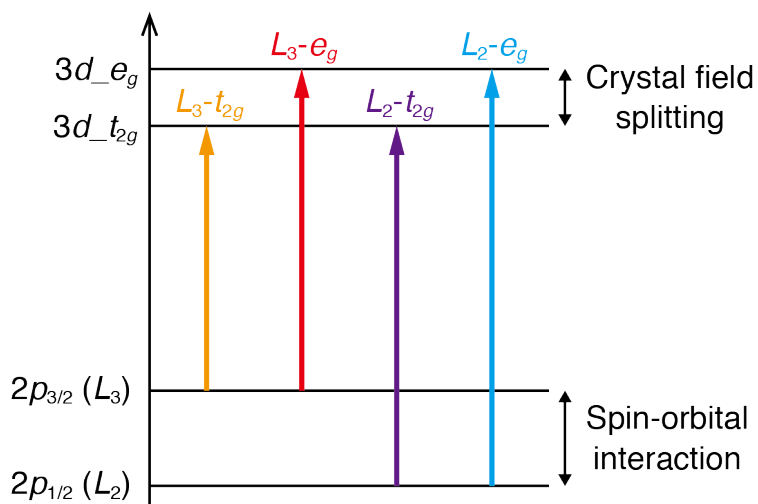
Figure 3-2. Schematic diagram of the transition processes for Ti *L*-edge XAS. Ti-2*p* initial states are split due to spin-orbital interaction, and Ti-3*d* final states are split due to the crystal field.
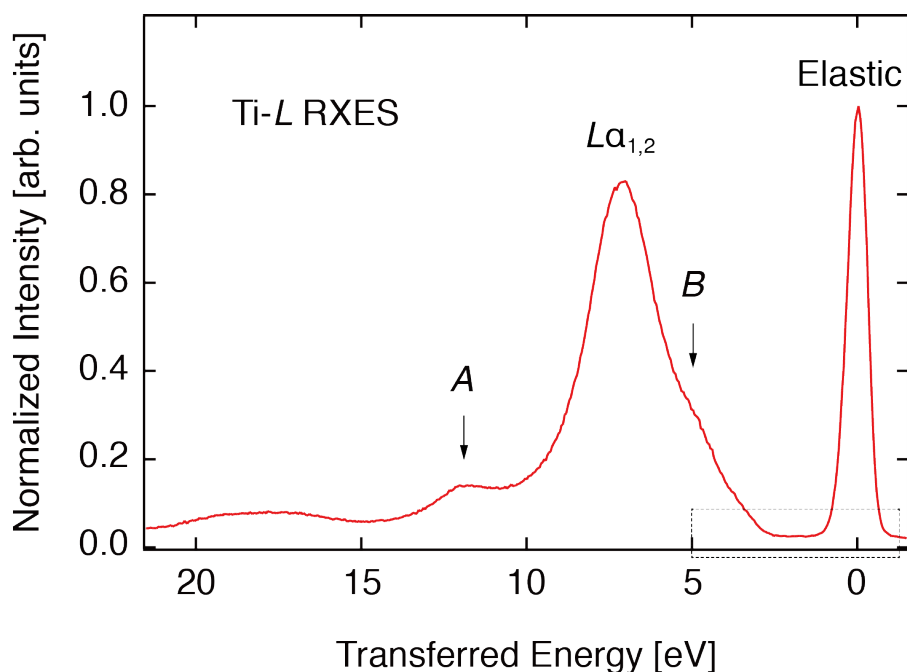
Figure 3-3. Ti-*L* RXES spectrum of a $SrTiO_3$ single crystal at low temperature. The excitation energy equals the Ti $L_3\_e_g$ absorption-edge energy labeled as *e* in **Figure 3-1**.

Figure 3-4 shows the intensity plot of the Ti-*L* RXES spectra. The horizontal and vertical axes are the excitation energy and the emission energy, respectively. The intensity plot demonstrates that the elastic scattering energy corresponds to the X-ray excitation energy. In **Figure 3-4**, the transferred energies of *A* and *B* features traced using the dashed lines are constant regardless of the excitation energy. This is called the Raman process, in which a photon loses a little energy by a certain excitation in a material. When the excitation energy is tuned to each charge-transfer satellite labeled as *m* and *o*, the *A* peak intensity increases resonantly, which can be indicated by the lower dashed line in **Figure 3-4**. Thus, *A* peak in the RXES spectra is due to charge transfer excitation, and from here the corresponding peak is referred as CT1. Shoulder structure *B* is faint, and it is difficult to identify its origin. Similar spectral features were observed

in the Ti-*L* RXES spectra of TiO$_2$. [2] The Raman peaks at E_{Tr} = 14 eV and 5–10 eV are caused by the electronic excitation to $d^1\underline{L}$ antibonding and nonbonding states. These features correspond to CT1 and to the shoulder in our spectrum.
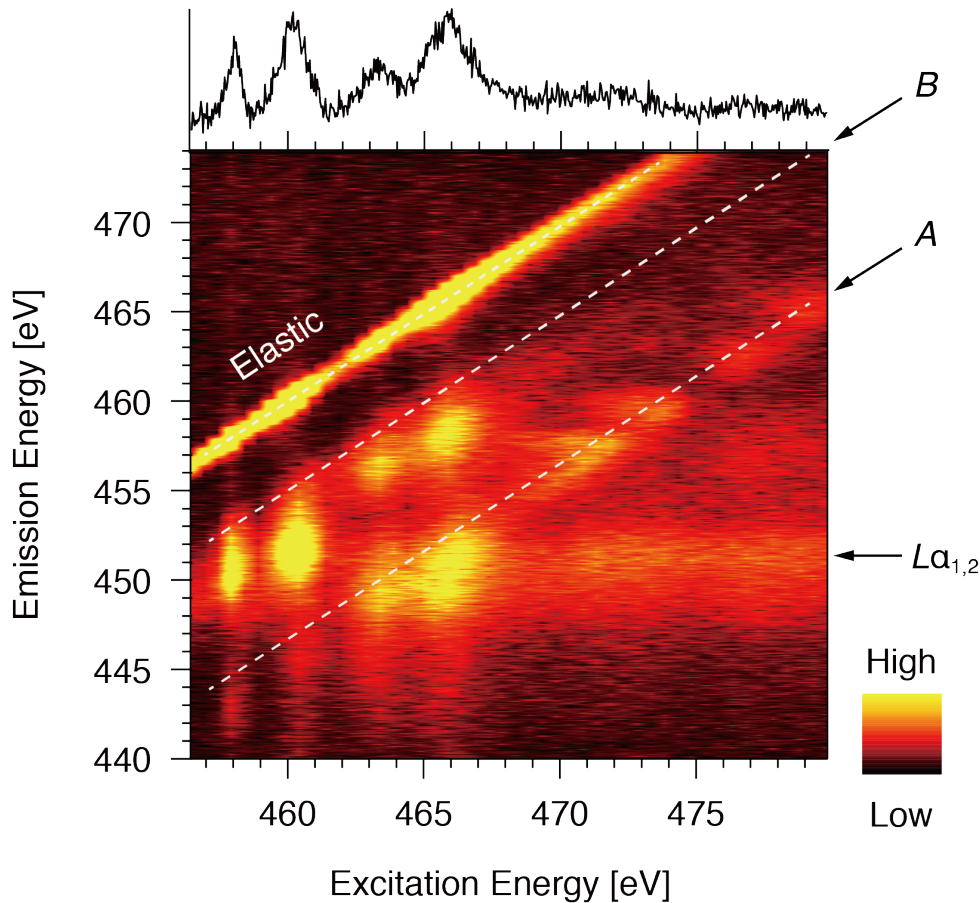
Figure 3-4. Intensity plot of the Ti-*L* RXES spectra. The horizontal and vertical axes are the excitation energy and the emission energy, respectively. The vertical slices correspond to the RXES spectra of different excitation energies. The two dashed lines indicate the traces of *A* and *B* peaks in **Figure 3-3**. The spectrum shown in the upper part of the intensity plot represents integration with respect to the emission energy.

3.1.3. Ti-*L* RXES Measurements of Electron-Doped SrTiO₃

Ti-*L* RXES is also implemented to perform measurements using electron-doped SrTiO$_3$ by substituting La for Sr with 5%. The excitation energy dependence of RXES at room temperature is shown in **Figure 3-5(a)**. The horizontal axis represents the emitted photon energy. The excitation X-ray energies of each spectrum correspond to the labels (*a–o*) in **Figure 3-1**. The main features are similar to those obtained using stoichiometric SrTiO$_3$. Furthermore, an additional peak is observed. **Figure 3-5(b)** depicts the enlarged view of the spectra between $L\alpha_{1,2}$ and elastic peaks excited by the energies of *a–e* in **Figure 3-1**. The small peak grows with the resonance of excitation energy at Ti $L_{3}\_e_g$ (*e*). The energy difference from the elastic peak is a constant value, which is close to the energy gap between Ti L_t_{2g} (*a*) and L_e_g (*e*) peaks in Ti-*L* XAS. This peak is also observed when the excitation energy it set to Ti $L_2\_e_g$ (*k*). We conclude that this is a *dd* excitation peak derived from crystal field excitation.

3.1.4. UV-induced *dd* excitation in Ti-*L* RXES

Figure 3-6 shows the enlarged Ti-*L* RXES spectra between the elastic and $L\alpha_{1,2}$ peaks. In stoichiometric SrTiO$_3$ at low temperature, a new Raman peak at $E_{Tr} = 2$ eV asymptotically increases in an exponential manner with time (blue line) under UV irradiation and remains after turning off UV irradiation. This peak is located at the energy position of *dd* peak obtained in electron-doped SrTiO$_3$.

A remarkable result is that *dd* peak appears in stoichiometric SrTiO$_3$ under UV irradiation only at low temperature. The emergence of *dd* peak indicates that *d* electrons are excited to nominal d^0 state in stoichiometric SrTiO$_3$. Under UV irradiation, electrons are transferred from O-2*p* states to Ti-3*d* states. Therefore, $d^1\underline{L}$ state is formed via *p–d*

hybridization and is strongly mixed with d^0 state owing to configuration interaction. The UV-enhanced hybridization would remain for a certain time as evidenced by the one-dimensional anharmonic vibration of Ti ions reported by Nozawa *et al.* [3] UV irradiation leads to reduction of the symmetry around a Ti^{4+} ion.
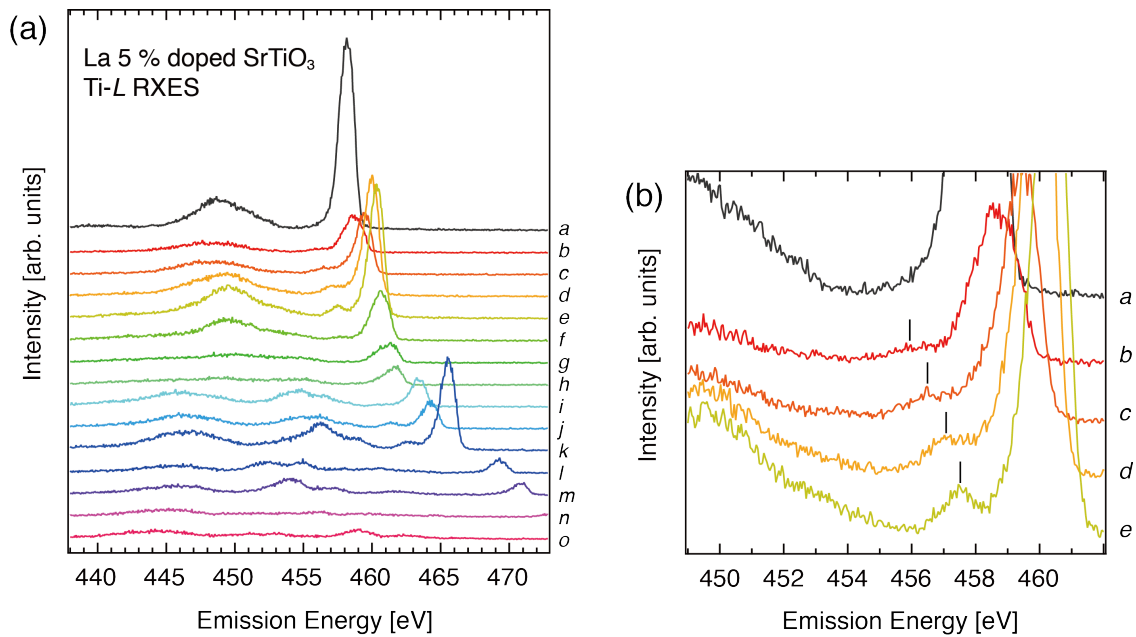
Figure 3-5. **(a)** Dependence of the Ti-*L* RXES spectra of La-doped SrTiO$_3$ on the excitation energy. **(b)** The enlarged view near the elastic peaks of **(a)** for the excitation corresponding to *a–e*.
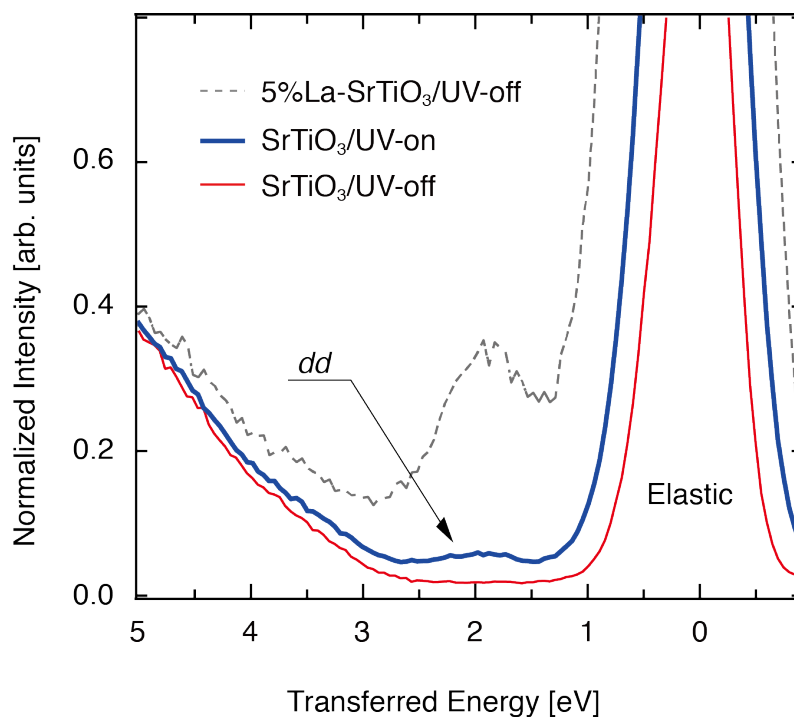
Figure 3-6. Dependence of the Ti-*L* RXES spectra on UV irradiation at low temperature. The spectrum of electron-doped SrTiO$_3$ is displayed as a reference. The excitation energy equals the Ti L_3_e_g absorption-edge energy labeled as *e* in **Figure 3-1**.

3.2. Ti *K*-edge XAS and RXES Measurements

3.2.1. Ti *K*-edge XAS Measurements

Figure 3-7 shows the Ti *K*-edge XAS spectrum of a SrTiO$_3$ single crystal at room temperature. The vertical bars with numbers (*#1* to *8*) denote the excitation energies of the Ti-*K*β RXES measurements. The excitation energy of the main Ti-*K*β RXES spectrum was 4.982 keV (*#3*), which is the energy of Ti-1s $\rightarrow$ 4p absorption edge. The weak features labeled as P_1, P_2, and P_3 represent the pre-edge structures. The two

former features arise from the electric quadrupole transition from Ti $1s$ to $3d$ (intra-atomic). The latter feature arises from the electric dipole transition from Ti $1s$ to $3d$ hybridized with $4p$ states (inter-atomic). [3, 4, 5] In particular, P_1 and P_2 originate from Ti-$3d\_t_{2g}$ and $3d\_e_g$ states, respectively.
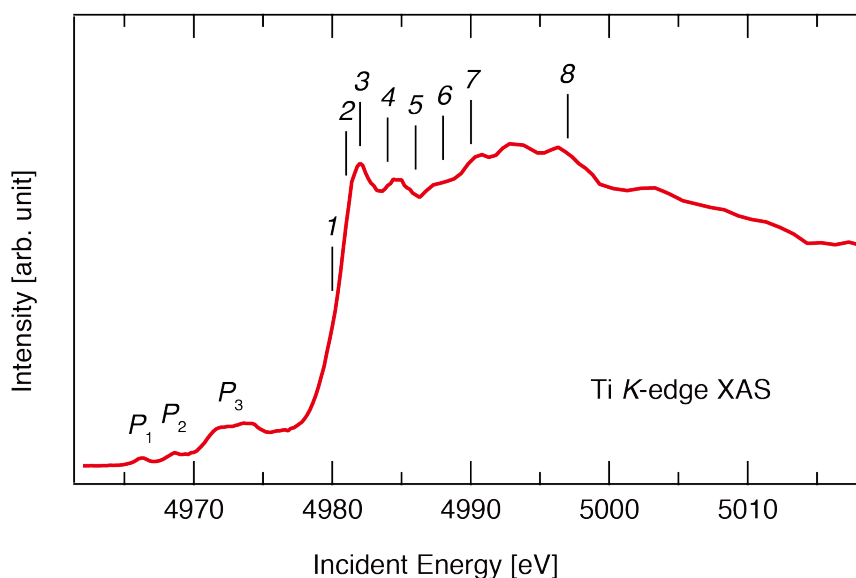
Figure 3-7. Ti K-edge XAS spectrum at room temperature. The vertical bars with numbers label the excitation energies of the Ti-$K\beta$ RXES measurements.

3.2.2. Ti-$K\beta$ RXES Measurements

The Ti-$K\beta$ RXES spectrum at 4 K is shown in **Figure 3-8** on a logarithmic scale. The horizontal axis represents the emitted photon energy. Except elastic scattering, three fluorescence peaks, $K\beta_{1,3}$, $K\beta''$, and $K\beta_{2,5}$, are observed. $K\beta_{1,3}$ peak is derived from

relaxation from occupied Ti-$3p$ state to $1s$ core hole. Satellite $K\beta''$ and $K\beta_{2,5}$ peaks are caused by hybridization between Ti and O orbitals. The former process is often attributed to the transition from the orbital related to O-$2s$ to $1s$ core hole, and the latter is attributed to the transition from O-$2p$ orbital hybridized with Ti-$3d$ orbital to $1s$ core hole. These fluorescence peaks also appear in other titanates such as $BaTiO_3$, [6, 7] TiO_2, and Ti_2O_3. [8]
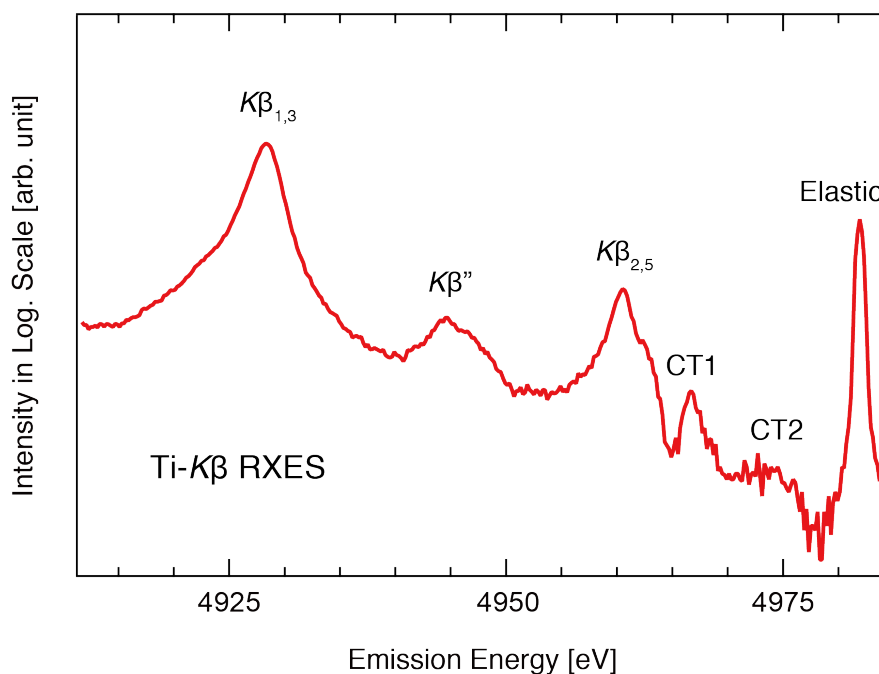
Figure 3-8. Ti-Kβ RXES spectrum excited at an energy of 4.982 keV (*#3* in **Figure 3-7**). The vertical axis is in logarithmic scale.

3.2.3. Excitation Energy Dependence of the Ti-*K*β RXES Spectra

Two slight features are located between the elastic and $K\beta_{2,5}$ peaks as shown in **Figure 3-8**. These features are the Raman peaks and are observed in other perovskite titanates, such as $BaTiO_3$, too. [6, 7] They are attributed to the charge transfer excitation between Ti and O in the TiO_6 octahedron. We label these peaks as CT1 and CT2 in order of increasing emission energy. Although the intensities of the CT peaks are significantly low compared with those of fluorescence peaks, the CT peaks are crucial to derive the atomic-scale information. In case of Ti-*K*β RXES, the CT peaks provide the information on the local electronic state around a Ti atom.

In order to prove that CT1 and CT2 peaks observed in $SrTiO_3$ are due to Raman processes, we show the excitation energy dependence of the RXES spectra in **Figure 3-9**. The horizontal axis represents the transferred energy. The excitation energies of each spectrum correspond to the numbers in **Figure 3-7**. The peak position of $K\beta_{2,5}$ fluorescence is shifted towards higher transferred energies if the excitation energy is increased as shown using the dashed line. In contrast, the CT peaks show constant transferred energies if the excitation energy is increased. CT1 peak is observed at $E_{Tr} =$ 15 eV in all spectra. CT2 peak is also observed at $E_{Tr} = 8$ eV when the excitation energies are set to the values corresponding to *#1–5*. The difference in the excitation energy region detecting CT1 and CT2 peaks depends on the resonance effect. A clear resonance effect of the CT peak is observed in other titanates. [2]
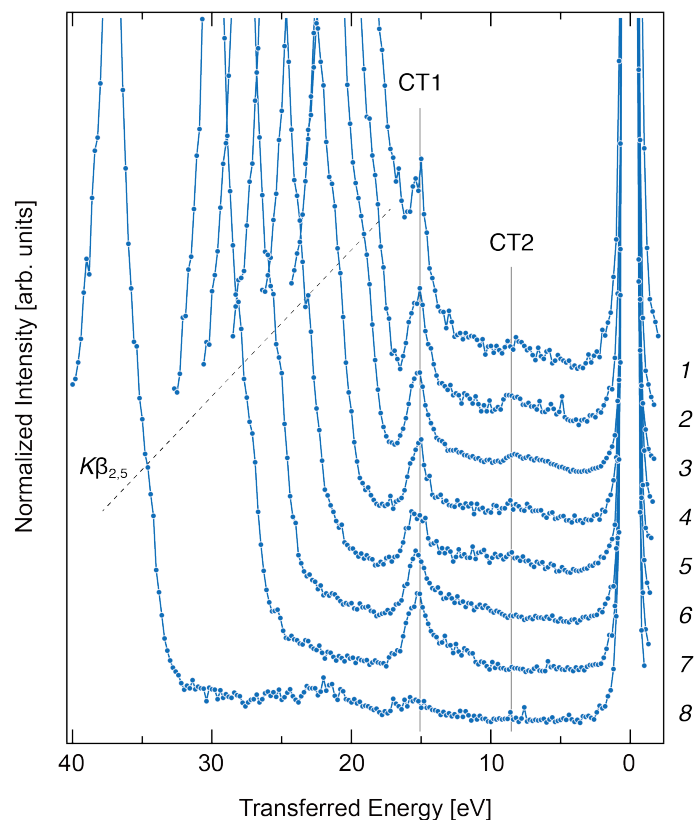
Figure 3-9. Dependence of the Ti-*K*β RXES spectra on the excitation energy. The numbers on the right side of each spectrum correspond to the excitation energies shown in **Figure 3-7**.

3.2.4. Polarization Dependence of Ti-*K*β RXES

Polarization dependence of the Ti-*K*β RXES spectrum was measured at an excitation energy of 4.982 keV (*#3*). The relation between photon polarization and measurement configuration is illustrated in **Figure 3-10(a)**. When the emitted photon polarization contains the same polarization direction of an incident X-ray, this geometry is referred to as "polarized configuration." On the other hand, when the emitted photon polarization rotates by 90º from that of the incident X-ray, this geometry is referred to as

"depolarized configuration." $K\beta_{2,5}$ fluorescence peak is detected in both configurations as shown in **Figure 3-10(b)**. In contrast, the CT peaks are not observed in the depolarized configuration. An elastic peak at $E_{Tr} = 0$ eV is not also detected in the depolarized configuration since elastic scattering follows the polarization configuration rule. The CT peaks show distinct polarization dependence. There are the independence of the CT peak position on the excitation energy and the polarization dependence of the CT peaks. Therefore, we conclude that CT1 and CT2 are Raman processes.

3.2.5. Temperature Dependence of the CT Peaks

The CT peaks are important for investigating the local electronic states of dielectric materials. In particular, CT2 peak is responsive to the local crystal structure and reflects the reaction to an external stimulus. We performed the Ti-$K\beta$ RXES measurements under various conditions to investigate the local structure and the origin of the electric polarization in $SrTiO_3$.

The Ti-$K\beta$ RXES spectra in the low-transferred energy region at room temperature are shown in **Figure 3-11**. CT1 peak is observed at $E_{Tr} = 15$ eV as during the measurements at 4 K, whereas CT2 peak is not observed (red circles). Under UV irradiation (blue diamonds), CT1 peak shows no changes, and no new features that exceed the spectral noise level are observed. These results indicate that CT2 peak appeared at 4 K as shown in **Figure 3-8** has the characteristic information on $SrTiO_3$ in the QPE phase. The sensitivity of CT2 peak makes probing slight variations in the local structure and in the electronic state induced by an external stimulus possible.
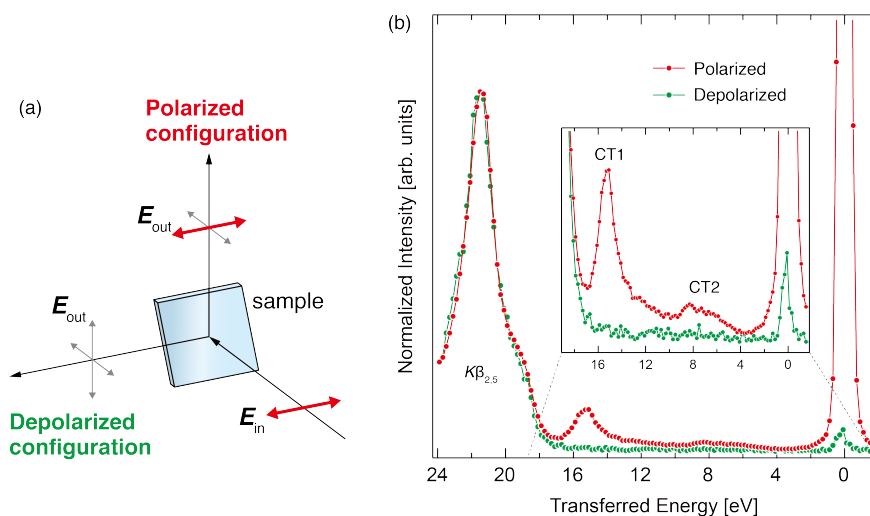
Figure 3-10. **(a)** Geometry of the polarization dependence measurement of Ti-*K*β RXES and its spectra **(b)** for the excitation corresponding to *#3*. The inset shows the enlarged spectra between the *K*β$_{2,5}$ and elastic peaks. No CT peak is observed in the depolarized configuration.
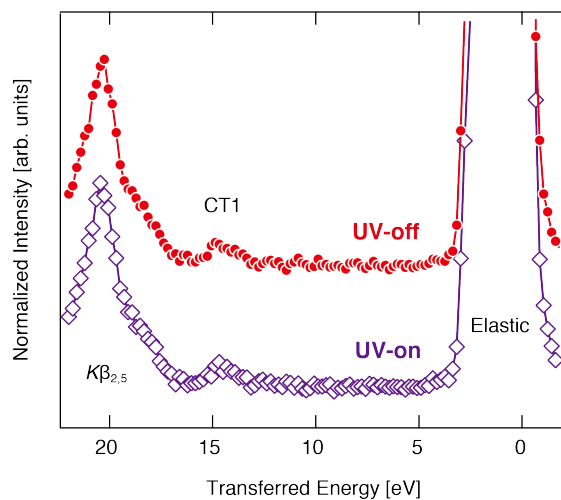
Figure 3-11. Dependence of the CT peaks on UV irradiation at room temperature. Neither CT2 peak nor new feature is appeared under UV irradiation.

3.2.6. Responses of the CT Peaks to UV Light and a DC Field

The responses of the CT peaks to UV light and a DC field at 4 K are depicted in **Figure 3-12**. On the top spectrum (red circles), CT2 peak has fine structures without UV irradiation or DC field application. We decomposed the CT features into five Gaussians: CT1, $CT2_A$, $CT2_B$, $CT2_C$, and $CT2_D$ components. The peak energy of each Gaussian is fixed since the lattice parameters are unchanged by external stimuli. [9] Only the electron occupation of the corresponding states is expected to change. With regard to the middle spectrum (blue diamonds), $CT2_A$ and $CT2_B$ intensities are decreased under UV irradiation. Moreover, we observe that $CT2_A$ and $CT2_B$ present an additional reduction in the intensity under UV irradiation and a DC field as shown in the bottom spectrum (green triangles).

The appearance of CT2 and its change induced by external stimuli indicate Ti off-center displacement. $CT2_A$ and $CT2_B$ peaks have high sensitivity to external stimuli and provide the information about the electronic state around a Ti atom, which we discussed below. In contrast, CT1, $CT2_C$, and $CT2_D$ show no change in their intensities and energies under UV irradiation or a DC field. The electric state corresponding to the CT peaks has already been revealed by our group [10] on the basis of the configuration interaction theory for a TiO_6 cluster. [11] The nominal valence number of Ti in $SrTiO_3$ is +4 with d^0 configuration. Under a cubic or tetragonal structure, the ground state and CT1 state are formed by hybridizing d^0 and $d^1\underline{L}$ states via p–d hybridization. Among $d^1\underline{L}$ states, a small portion remains unhybridized to create CT2 state at the energy level between the ground state and CT1 state. In particular, CT2 state disappears under the condition of the perfect cubic symmetry as shown in the Ti-$K\beta$ RXES spectrum at room temperature (**Figure 3-11**).
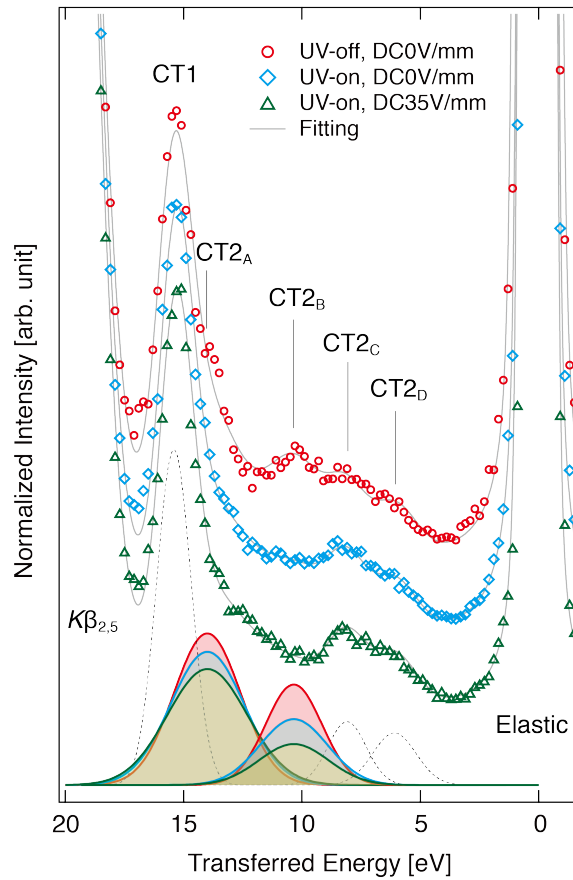
Figure 3-12. Ti-*K*β RXES spectra between the elastic and *K*β$_{2,5}$ peaks at 4 K and the dependence of the CT peaks on external stimuli. All CT peaks are fitted using several Gaussians.

3.3. Effect of External Stimuli in the QPE Phase

3.3.1. Local Polar Region

We discuss the local polar region in a SrTiO$_3$ single crystal through the behavior of CT2 peak. No CT2 peak is observed at room temperature regardless of the presence of

UV irradiation. SrTiO$_3$ has extremely high crystal symmetry ($Pm\bar{3}m$) at room temperature. A Ti atom is located at the body center site of the TiO$_6$ octahedron in the paraelectric phase. Hence, no local polar region is induced leading to the absence of CT2 peak at room temperature.

In contrast, the appearance of CT2 peak at 4 K results from a reduction in the crystal symmetry, especially around a Ti atom, owing to the structural phase transition at 105 K. SrTiO$_3$ remains in the paraelectric state below the structural phase transition point because the formation of the ferroelectric order is prevented by a quantum fluctuation. However, in terms of the microscopic structure, a Ti atom cannot remain at the body center site of the TiO$_6$ octahedron because of a slight local lattice distortion, as schematically illustrated by small off-centering in **Figure 3-13(a)**. Indeed, SrTiO$_3$ has a small tetragonal distortion below the structural phase transition point, the coordination environment around a Ti atom is unstable. Therefore, Ti off-center displacement that is the electric dipole moment exists behind quantum fluctuations at low temperature. A tiny change lying behind the macroscopic structure can be revealed by the electronic state observation through CT2.

Here, we recall the fitting results shown in **Figure 3-12**. CT1 and CT2 peaks together with the large elastic and $K\beta_{2,5}$ slopes are decomposed by five Gaussians. The magnitudes of CT2$_A$ and CT2$_B$ components are diminished by UV irradiation at 4 K. In the low temperature region as shown in **Figure 3-13(a)**, the polar region is expected to develop owing to a perturbation larger than the quantum fluctuation. According to previous researches, UV light serves as a stimulus that shifts the stable position of a Ti atom towards the off-center sites along the Ti–O bonds. [12, 13] Ti off-centering is enlarged under UV irradiation at low temperature. Therefore, we conclude that the UV-induced decreases in CT2$_A$ and CT2$_B$ components indicate a significant Ti off-center displacement, as shown in **Figure 3-13(b)**. However, the Ti displacements are not aligned in the same direction since our UV light is not polarized. Therefore, the

electric dipole moments are introduced in random directions. Ferroelectric long-range order is not realized by UV irradiation alone. UV irradiation forms the local polar regions composed of the Ti displacements that easily evolve into ferroelectric domains if an additional stimulus is applied.

Further reductions in $CT2_A$ and $CT2_B$ components occur under a DC field along with UV irradiation. The direction of the DC field is parallel to that of the Ti–O bond, which is one of the six directions of the UV-assisted Ti off-center displacements. The change in $CT2_A$ and $CT2_B$ components induced by DC field application corresponds to the alignment of the Ti off-center displacements [**Figure 3-13(c)**]. The DC field aligns the UV-assisted electric dipole moments in parallel and leads to the enlargement of the polar regions. To ensure this scenario, we also measured the Ti-$K\beta$ RXES spectrum under DC field application at 4 K without UV irradiation and found no spectral change. Thus, Ti off-center displacement is not introduced by the DC field application alone.

3.3.2. Macroscopic Dielectric Properties

In this section, we discuss macroscopic properties of the UV-assisted electric-dipole moments. In previous researches, it was expected that the photoinduced polar region was developed under UV irradiation, which lead to the giant dielectric constant with a bias DC field. [14, 15] In the present RXES study, we reveal a substantial evidence of the presence of this microscopic polar region composed of UV-assisted the Ti off-center displacements or the electric dipole moments. However, compared with case of typical ferroelectric materials, dipole–dipole interaction between the moments is weak in $SrTiO_3$ owing to a small double-well potential. [16] Therefore, the long-range order of the UV-induced moments is prevented by thermal or zero-point fluctuations. In fact, the first-order transition of the dielectric constant at the Curie temperature, which is the

characteristic of displacive-type ferroelectric materials, is not observed in $SrTiO_3$ under UV irradiation and a DC field. In order to verify the effect of these fluctuations, the temporal evolution of the UV+DC-induced polar region must be examined via time-resolved X-ray spectroscopy.

(a)

4 K (QPE)

(b)

UV

4 K + UV

(c)

E

4 K + UV + DC
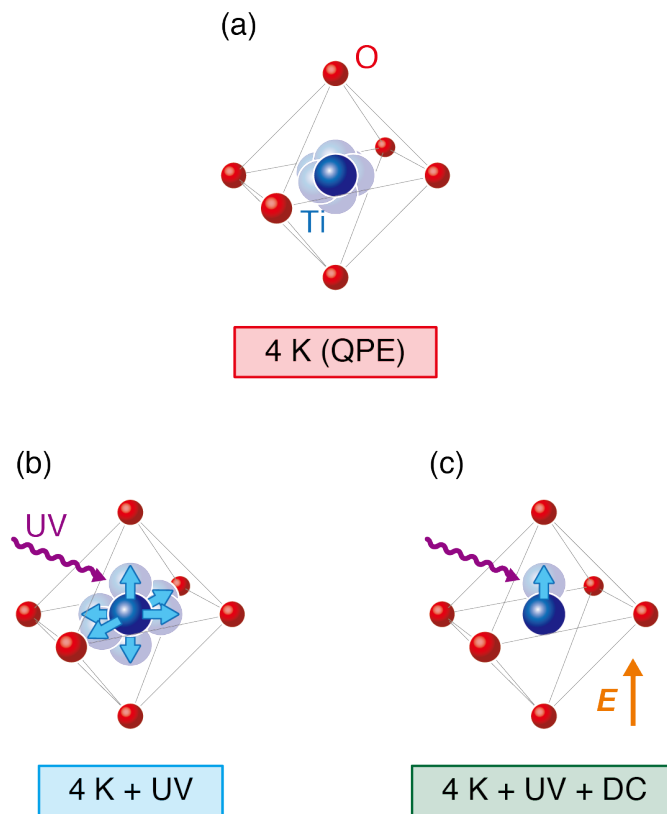
Figure 3-13. Schematic diagrams of Ti off-center displacement in the TiO_6 octahedron induced by external stimuli. **(a)** At 4 K, a Ti atom is displaced from the body center site of the TiO_6 octahedron due to a slight local lattice distortion. **(b)** UV irradiation assists a significant Ti off-centering along the six equivalent Ti–O directions at 4 K. **(c)** The UV-assisted displacements are aligned by a DC field (*E*). UV irradiation and DC field application introduce a local polar region in a $SrTiO_3$ single crystal in the QPE phase.

Bibliography

[1]   Y. Tezuka, N. Nakajima, and O. Morimoto: J. Electron Spectrosc. Relat. Phenom. **184**, 216 (2011).

[2]   Y. Harada, T. Kinugasa, R. Eguchi, M. Matsubara, A. Kotani, M. Watanabe, A. Yagishita, and S. Shin: Phys. Rev. B **61**, 12854 (2000).

[3]   S. Nozawa, T. Iwazumi, and H. Osawa, Phys. Rev. B **72**, 121101(R) (2005).

[4]   J. Danger, P. Le Fèvre, H. Magnan, D. Chandesris, S. Bourgeois, J. Jupille, T. Eickhoff, and W. Drube, Phys. Rev. Lett. **88**, 243001 (2002).

[5]   T. Uozumi, A. Kotani, and J. C. Parlebas, J. Electron Spectrosc. Relat. Phenom. **137–140**, 623 (2004).

[6]   Y. Isohama, N. Nakajima, G. Watanabe, M. Mizumaki, N. Kawamura, and H. Maruyama, Jpn. J. Appl. Phys. **50**, 09NE04 (2011).

[7]   Y. Isohama, N. Nakajima, H. Maruyama, Y. Tezuka, and T. Iwazumi, J. Electron Spectrosc. Relat. Phenom. **184**, 207 (2011).

[8]   L. Mandić, S. Fazinić, and M. Jakšć, Phys. Rev. A **80**, 042519 (2009).

[9]   N. Nakajima, M. Deguchi, H. Maruyama, H. Osawa, C. Moriyoshi, and Y. Kuroiwa, Jpn. J. Appl. Phys. **52**, 09KF05 (2013).

[10]   N. Nakajima, M. Oki, Y. Isohama, H. Maruyama, Y. Tezuka, K. Ishiji, T. Iwazumi, and K. Okada, Phys. Rev. B **86**, 224114 (2012).

[11]   K. Okada and A. Kotani, J. Electron Spectrosc. Relat. Phenom. **62**, 131 (1993).

[12]   S. Nozawa, T. Iwazumi, and H. Osawa, Phys. Rev. B **72**, 121101(R) (2005).

[13]   S. Nozawa, T. Iwazumi, H. Osawa, and T. Uozumi, Appl. Phys. Express **6**, 061501 (2013).

[14]   M. Takesada, T. Yagi, M. Itoh, and S. Koshihara, J. Phys. Soc. Jpn. **72**, 37 (2003).

54

[15] T. Hasegawa, S. Mouri, Y. Yamada, and K. Tanaka, J. Phys. Soc. Jpn. **72**, 41 (2003).

[16] T. Nishimatsu, M. Iwamoto, Y. Kawazoe, and U. V. Waghmare, Phys. Rev. B **82**, 134106 (2010).

4. Conclusion

In the present study, we examined the origin of the photoinduced electric dipole moment in a SrTiO$_3$ single crystal in the quantum paraelectric (QPE) phase using resonant X-ray emission spectroscopy (RXES). The results can be summarized as follows:

- **Electronic state observation around a Ti atom**

Ti-*L* and *K*β RXES measurements were performed on a SrTiO$_3$ single crystal at low temperature. In Ti-*L* RXES measurements, the crystal field excitation (*dd*) peak, which means the existence of *d* electrons, was observed under ultraviolet (UV) irradiation. This result indicates that electrons are transferred from O-2*p* states to Ti-3*d* states under UV irradiation.

The X-ray Raman peaks derived from the charge transfer (CT) excitation between Ti-3*d* and O-2*p* orbitals were observed using Ti-*K*β RXES measurements. UV irradiation and direct-current (DC) electric field application decreased CT2$_A$ and CT2$_B$ intensities, which were not observed at room temperature. These peak reductions mean that change in *p*–*d* hybridization between Ti-3*d* and O-2*p* orbitals is affected by UV irradiation.

- **Ti off-center displacement in the TiO$_6$ octahedron**

The appearance of CT2 peak in the Ti-*K*β RXES spectra at 4 K shows that a Ti atom is displaced from the body center site of the TiO$_6$ octahedron. From the reduction of CT2$_A$ and CT2$_B$ intensities under UV irradiation, the Ti off-center displacement, i.e., the

electric dipole moment in a unit cell, is enhanced along the Ti–O direction under UV irradiation. In addition, the Ti-*L* RXES measurements also indicate that UV irradiation leads to a reduction of the symmetry around a Ti atom due to the change of the *d*-electron number. The results of the Ti-*L* RXES measurements support UV-induced change in the Ti-*K*β RXES spectra.

- **Photoinduced polar region**

From the additional reduction of $CT2_A$ and $CT2_B$ intensities under UV irradiation and a DC field, the UV-assisted electric dipole moments are aligned parallel to the applied DC field. Furthermore, Ti off-center displacement is not enhanced by DC field application alone. The applied DC field enlarges the photoinduced polar regions. Therefore, we successfully reveal a substantial evidence of the local polar region introduced by external stimuli in a $SrTiO_3$ single crystal in the QPE phase.

For quantum paraelectric $SrTiO_3$, a local polar region lying behind the macroscopic structure was clarified from X-ray Raman features, *dd* and CT excitations, in the RXES spectra. A great advantage of RXES measurements is that the hybridized electronic state around a specific atom can be observed under external stimuli. Therefore, the transformation of Ti off-center displacement is investigated by controlling external stimuli. In this study, it was demonstrated that the electronic state observation using RXES contributes to researches on the microscopic nature of dielectric materials.

Acknowledgments

Mr. A. Sano, Mr. C. Temba, Mr. K. Moriai, Mr. T. Naito, Mr. Y. Nakamura, Mr. K. Mine, Mr. S. Ono, Mr. Y. Yamanaka, Mr. K. Yokoyama, and my seniors and juniors. I will always remember how we worked hard together and had a pleasant time. I am hopeful for their success.

Finally, I would like to express my special thanks for my family.

January 2016
Shuhei Kawakami